Journal of *Marine Science and Engineering*

MDPI

Article

A Control-Oriented Thruster Management Framework for Fault-Tolerant Propulsion of Remotely Operated Vehicles

Lu Wang [1,†], Yi Wu [1,†], Chao Fang [2], Jie Gao [1], Yonggang Gu [3], Chao Zhai [3,*] and Zhen Zhang [4,*]

[1] Institute of Advanced Technology, University of Science and Technology of China, Hefei 230027, China; wanglu_space@mail.ustc.edu.cn (L.W.); wuyii@mail.ustc.edu.cn (Y.W.)
[2] School of Engineering Science, University of Science and Technology of China, Hefei 230027, China
[3] Experimental Center of Engineering and Materials Science, University of Science and Technology of China, Hefei 230027, China
[4] Department of Precision Machinery and Precision Instrumentation, University of Science and Technology of China, Hefei 230027, China
* Correspondence: zhaichao@ustc.edu.cn (C.Z.); zhen051@ustc.edu.cn (Z.Z.)
† These authors contributed equally to this work.

Abstract

Remotely operated vehicles (ROVs) typically rely on over-actuated propulsion systems to achieve precise dynamic positioning and maneuvering in complex underwater environments. In practice, however, conventional propulsion management based on thrust allocation is often challenged by non-ideal actuator behaviors, such as cavitation-induced thrust degradation, low-speed dead-zone effects, inter-thruster coupling, and partial actuator failures. Most existing approaches treat propulsion management as a static force distribution problem and implicitly assume ideal or fast thrust execution, which limits performance when actuator dynamics and execution uncertainty become significant. To address these limitations, this paper proposes a control-oriented thruster management framework that reformulates propulsion management as a feedback regulation problem rather than a static allocation task. In the proposed framework, actuator dynamics and thrust execution uncertainty are explicitly incorporated into the control loop. At the actuator level, thrust degradation and low-speed operation are compensated through disturbance-aware feedback control, while at the system level an LQI-based controller with thrust response compensation is employed to coordinate multi-degree-of-freedom (DOF) force and moment regulation and suppress cross-axis coupling. Fault tolerance is achieved inherently through feedback regulation without relying on explicit fault detection or reallocation. Experimental results obtained from an ROV propulsion platform, including single-thruster tests, coupled multi-DOF control, and a thruster shutdown scenario, demonstrate improved thrust executability, reduced coupling-induced disturbances, and enhanced fault-tolerant performance compared with conventional direct thrust allocation strategies.

Keywords: remotely operated vehicle (ROV); thruster management; fault-tolerant control

Academic Editor: Alon Gany

Received: 14 January 2026
Revised: 4 February 2026
Accepted: 9 February 2026
Published: 12 February 2026

1. Introduction

Dynamic positioning (DP) is a fundamental capability for remotely operated vehicles (ROVs) [1–4], enabling precise station keeping and trajectory tracking during underwater inspection, manipulation, and intervention tasks. With the increasing deployment of ROVs in shallow-water operations, subsea infrastructure inspection, and confined marine environments, propulsion systems are required to deliver not only accurate force and

moment control but also strong robustness against actuator nonlinearities, disturbances, and faults. In practice, modern ROVs are typically equipped with over-actuated propulsion systems, where redundant thrusters are employed to ensure maneuverability and fault tolerance across multiple degrees of freedom (DOFs) [5]. In practical marine environments, ROV propulsion systems are typically implemented using multiple electrically driven thrusters, such as ducted or tunnel-type propellers optimized for low-speed and high-thrust operation. These thrusters are commonly arranged in symmetric configurations, for example with horizontal-plane thrusters generating surge, sway, and yaw forces, and vertical-plane thrusters providing heave and attitude control. Such configurations are intentionally designed to be over-actuated in order to enhance maneuverability and fault tolerance. However, the geometric arrangement and redundancy of thrusters also introduce strong coupling effects among different degrees of freedom, making reliable force and moment generation highly dependent on propulsion management strategies, especially under non-ideal underwater operating conditions.

In conventional DP architectures, the propulsion system is usually organized in a cascaded manner, consisting of a high-level motion controller and a thruster allocation (TA) module [6,7]. The TA module maps the commanded forces and moments into individual thruster commands, commonly formulated as an optimization problem [8]. Existing TA approaches can be broadly categorized into planning-based methods, such as pseudo-inverse and quadratic programming, and metaheuristic-based methods, including genetic algorithms and particle swarm optimization [9–13]. While these approaches offer flexibility in handling constraints and redundancy, they typically assume that individual thrusters behave as ideal, fast-response actuators. This assumption becomes increasingly questionable in real underwater environments, where actuator dynamics, nonlinearities, and environmental interactions significantly influence thrust executability [14,15].

In the existing literature on ROV propulsion management, research efforts have predominantly focused on thrust allocation, redundancy resolution, and fault-tolerant strategies based on diagnosis, reconfiguration, or switching among predefined allocation schemes. In these approaches, thrusters are commonly modeled as static or weakly dynamic force generators, and their dynamic characteristics are typically treated outside the system-level feedback loop. Consequently, control-oriented formulations that explicitly incorporate thruster dynamics into feedback regulation remain relatively limited in underwater robotic applications [16]. By contrast, in many robotic control problems involving complex actuators, such as robotic manipulators operating under impedance or force control frameworks, actuator dynamics are routinely accounted for and embedded within closed-loop control design [17]. This contrast suggests that revisiting ROV propulsion management from a control-oriented perspective may offer a complementary framework when thrust execution uncertainty and dynamic effects play a significant role.

Underwater thrusters driven by sensorless field-oriented control (FOC) brushless motors exhibit several non-ideal characteristics that challenge this assumption. In shallow-water conditions, cavitation can induce severe and rapidly varying thrust degradation, leading to large force fluctuations that cannot be effectively compensated by speed control alone [18]. Moreover, underwater thrusters commonly suffer from low-speed dead-zone behavior, which restricts the generation of small control forces and degrades fine positioning performance [19]. These effects are further aggravated by the lack of direct thrust or rotor position measurements in sensorless drive systems. As a result, thrust commands generated by conventional TA schemes may not be faithfully executed at the actuator level, causing noticeable performance degradation at the system level.

Another critical challenge in over-actuated ROV propulsion systems is fault tolerance. Thruster faults may occur abruptly due to electrical, mechanical, or environmental

causes, posing a serious threat to operational safety [20–22]. Many existing fault-tolerant TA strategies rely on explicit fault detection, isolation, and reconfiguration or repeated optimization, which increases system complexity and computational burden. For embedded ROV platforms with limited onboard resources, such approaches may compromise real-time performance and reliability. From a control perspective, there is a strong motivation to develop propulsion control frameworks that can inherently absorb actuator degradation and partial failures through feedback regulation, without relying on explicit fault identification [23].

Motivated by these challenges, this paper reformulates thruster allocation from a static force distribution problem into a control-oriented thrust management problem, in which actuator dynamics and coupling effects are explicitly incorporated into the feedback loop. At the actuator level, cavitation-induced thrust degradation is mitigated by regulating thrust indirectly through load torque control, supported by an extended state observer (ESO) that estimates unmeasured load disturbances in real time [24–26]. Low-speed dead-zone behavior is alleviated by intentional d-axis current injection, which enhances electrical damping and observability in sensorless FOC drives, thereby extending the stable operating range of underwater thrusters [27]. At the system level, the over-actuated propulsion system is treated as a multi-input multi-output (MIMO) dynamic system rather than a static allocator, and a linear–quadratic–integral (LQI) controller augmented with ESO-based thrust response compensation is developed to achieve coordinated multi-DOF force and moment regulation [28–30].

Overall, this paper proposes a control-oriented thruster management framework for over-actuated ROV propulsion systems that explicitly integrates actuator dynamics into the feedback control loop. Cavitation-induced thrust degradation in shallow-water operations is mitigated by regulating thrust indirectly through load torque control supported by an ESO, enabling robust thrust execution without direct thrust sensing. Low-speed dead-zone behavior in sensorless underwater thruster drives is alleviated via intentional d-axis current injection, which enhances electrical damping and observability and extends the stable operating range toward near-zero speeds. At the system level, thruster allocation is reformulated as a dynamic multi-input multi-output control problem, and a linear–quadratic–integral controller augmented with ESO-based thrust response compensation is developed to improve multi-DOF coordination, suppress cross-axis coupling, and provide inherent fault tolerance under thruster degradation or failure. The effectiveness of the proposed framework is validated through comprehensive experiments on an ROV propulsion platform, covering single-thruster behavior, coupled multi-DOF control, and fault-tolerant operation scenarios.

The remainder of this paper is organized as follows. Section 2 introduces the actuator-level characteristics of underwater thrusters and the corresponding control strategies. Section 3 presents the proposed control-oriented thruster management framework and the associated system-level control design. Section 4 reports the experimental results obtained under representative operating conditions, including coupled multi-degree-of-freedom control and fault scenarios. Section 5 provides a detailed discussion and interpretation of the experimental findings. Finally, Section 6 concludes the paper and outlines future research directions.

2. Control Strategies for Underwater Thrusters

2.1. Cavitation Effects in Shallow Water

In shallow-water operations, cavitation inevitably causes propellers to ingest surrounding air during high-speed rotation, forming complex vortex structures. This phenomenon not only leads to significant thrust fluctuations but also generates intense noise. Under con-

stant rotational speed, the thrust output of each propeller exhibits considerable variability. As rotational speed increases, noise and thrust oscillations become more pronounced, as shown in Figure 1a. ROVs are typically ballasted to naturally float at the water surface. However, deviations in initial pitch and roll angles from the nominal state can cause some propellers to partially emerge from the water, exacerbating cavitation effects. Thrust loss near the water surface is difficult to quantify, and inconsistencies in thrust generation among propellers can lead to significant thrust discrepancies, as illustrated in Figure 1b. This directly causes instability in the ROV's structure, resulting in fluctuations in its attitude and position.

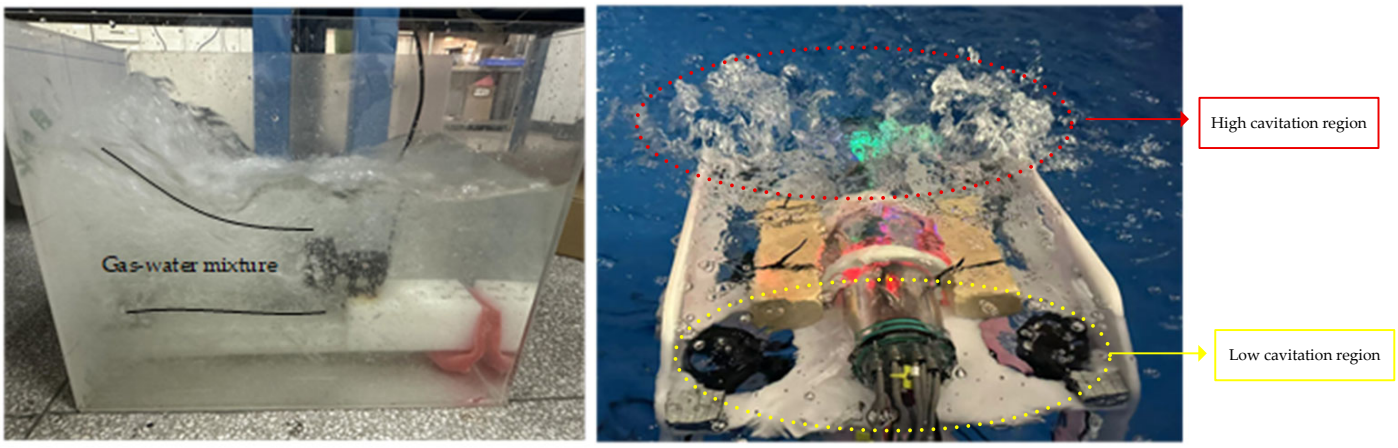

(**a**) (**b**)

Figure 1. Cavitation in shallow-water thruster operation: (**a**) single thruster cavitation near the surface; (**b**) ROV stability impact from cavitation-induced thrust loss.

In underwater operations, propellers are driven by brushless motors to generate thrust. The expressions for thrust and torque are as follows [31]:

$$\begin{cases} F = K_f \rho \omega_m^2 D^4 \mathrm{sgn}(\omega_m) \\ T_l = K_l \rho \omega_m^2 D^5 \mathrm{sgn}(\omega_m) \end{cases} \tag{1}$$

where F (N) denotes the generated thrust, T_l (N·m) represents the hydrodynamic load torque, K_f and K_l are the thrust and torque coefficients, respectively, ρ (kg·m^{-3}) is the fluid density, D (m) is the propeller diameter, ω_m (rpm) denotes the propeller angular velocity, and $\mathrm{sgn}(\cdot)$ is the sign function indicating the rotation direction.

Load integral compensation is employed as a velocity feedforward compensation term to address the thrust loss caused by cavitation. An inherent correlation exists between load torque and velocity control: compensating the velocity control loop using load torque can reduce the order of the velocity control loop. Based on the idea of optimizing the velocity control loop into a first-order inertial element, a proportional–integral (PI) controller can be introduced to directly regulate the load torque, thereby significantly improving the robustness of the system.

A second-order extended state observer (ESO) is designed for load torque estimation, with its operating principle given by [32]:

$$\begin{cases} \dot{\hat{\omega}}_m = J^{-1}\left(T_e - \hat{T}_l - b_m \hat{\omega}_m\right) + \lambda_1 \hat{e}_\omega \\ \dot{\hat{T}}_l = J \lambda_2 \hat{e}_\omega \end{cases} \tag{2}$$

where $\hat{\omega}_m$ denotes the estimated rotor speed, J is the rotor inertia, T_e is the electromagnetic torque, b_m is the viscous damping coefficient, $\hat{T}_l$ is the estimated load torque, $\hat{e}_\omega$ represents

the speed estimation error, and λ_1, λ_2 are the observer gains of the ESO. The convergence of the proposed ESO is based on the standard assumption that the load disturbance varies slowly, for example, $|\dot{T}_l| \leq \varepsilon_1$; here, ε_1 is an unknown yet finite positive constant. Under this assumption, the ESO is stable and the estimation error is bounded. The speed control loop controller is designed via load torque compensation and order reduction of the speed control loop, with its specific implementation given by

$$\begin{cases} e_\omega = \omega_m^* - \omega_m \\ i_q^* = k_{p\omega} e_\omega + \dfrac{\hat{T}_l}{1.5 p_n \varphi_{\text{flux}}} \end{cases} \tag{3}$$

where e_ω denotes the speed tracking error, i_q^* is the q-axis current reference, $k_{p\omega}$ is the proportional gain of the speed loop, p_n is the number of pole pairs, and φ_{flux} is the flux linkage constant. Based on Equations (1)–(3), the control law for load torque control is designed:

$$\begin{cases} e_l = T_l^* - \hat{T}_l \\ \omega_m^* = k_{pl} e_l + \int k_{il} e_l dt \end{cases} \tag{4}$$

where e_l is the load torque error; T_l^* is the load torque reference; and k_{pl} and k_{il} represent the PI loop parameters.

The load torque control loop is constructed using load torque information, and the load torque is used to compensate the speed loop. The control block diagram is shown in Figure 2:

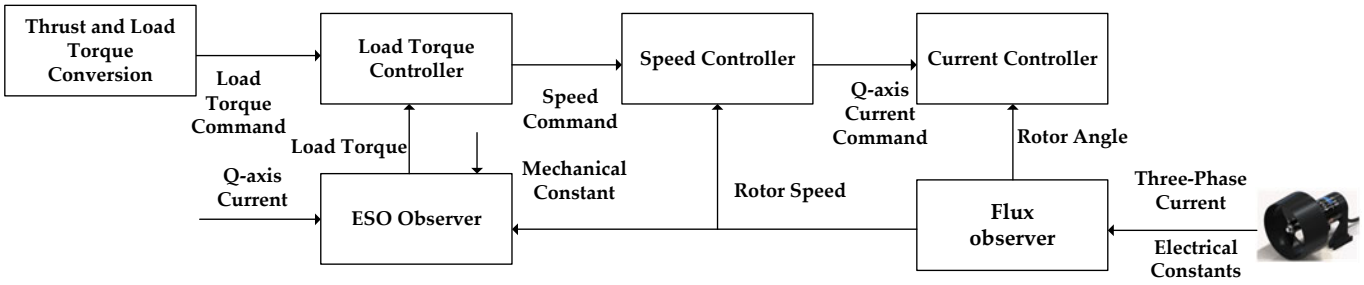

Figure 2. Block diagram of the load-torque-based thruster control.

2.2. Injection of D-Axis Current Method

Sensorless field-oriented control (FOC) is widely adopted in underwater thrusters due to its hardware simplicity and reliability. However, sensorless schemes generally suffer from degraded performance at low rotational speeds, where current signals become weak and highly susceptible to noise, making accurate rotor position estimation difficult. In ROV operations, this limitation is further exacerbated by the dead-zone characteristics of underwater thrusters, which restrict the generation of effective thrust at low speeds and hinder fine attitude and position adjustments.

For surface-mounted PMSM without salient pole characteristics, conventional FOC strategies typically set the d-axis current to zero to achieve maximum torque per ampere (MTPA). Under low-speed conditions, the required q-axis current is small, resulting in a low signal-to-noise ratio for electrical angle estimation. Consequently, the estimated reference frame often lags behind the actual rotor reference frame, as illustrated in Figure 3. This phase lag directly affects electromagnetic torque generation and may lead to torque attenuation or oscillatory behavior.

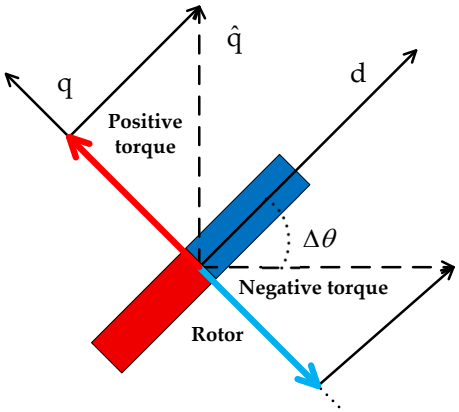

Figure 3. D-axis current injection in sensorless FOC.

Considering the phase deviation between the estimated and actual reference frames, the electromagnetic torque can be expressed as [27]

$$T_e = 1.5 * p_n * \varphi_{\text{flux}}(\hat{i}_q \cos(\Delta\theta) + \hat{i}_d \sin(\Delta\theta)) \quad (5)$$

where $\hat{i}_d$ and $\hat{i}_q$ are the estimated d-axis and q-axis currents, and $\Delta\theta$ denotes the phase estimation error. When the nonlinear flux observer converges and the phase deviation varies slowly, higher-order nonlinear terms can be neglected, allowing a simplified low-speed dynamic model to be derived. Under these conditions, the resulting system dynamics exhibit reduced damping, which contributes to the observed dead-zone behavior.

To alleviate this limitation, a controlled d-axis current is intentionally injected at low rotational speeds. Rather than aiming to increase torque output directly, the injected d-axis current modifies the effective damping characteristics of the motor drive and enhances the observability of the electrical states. This improves the robustness of rotor position estimation and stabilizes electromagnetic torque generation near zero speed.

It is important to note that the role of d-axis current injection in this work is not to claim an inherent improvement in torque efficiency, but to mitigate the dead-zone phenomenon that limits the executability of small control commands. By providing sufficient electrical excitation and damping, the proposed method establishes a necessary actuator-level condition for stable low-speed thrust regulation. The effectiveness of this approach is further examined through experimental results in Section 4.2.

It should be noted that the purpose of the d-axis current injection in this work is to enhance system observability and stability under low-speed operating conditions, where back-EMF is insufficient for reliable sensorless estimation. In medium- and high-speed regimes, the proposed control framework does not require d-axis current injection, and the injected current can be reduced or eliminated accordingly. It is acknowledged that d-axis current injection introduces additional copper losses and may lead to increased thermal stress; however, this trade-off is inherent to sensorless low-speed operation and is justified by the significant improvement in thrust stability and controllability in near-zero-speed conditions. In practical implementation, the injection magnitude is limited to a small range and activated only when low-speed operation is detected.

3. Fault-Tolerant Thruster System

3.1. ROV Thruster Configuration

The thrust of an ROV is generated by multiple thrusters, and their configuration determines the thrust and torque each thruster produces. Take an ROV with eight thrusters in a six-degree-of-freedom configuration as an example; the thrusters are distributed across vertical and horizontal planes. A coordinate system is established with the ROV's center of

mass as the origin, as shown in Figure 4. To facilitate subsequent modeling of force and moment synthesis, the geometric parameters and installation angles of all thrusters are explicitly summarized in Table 1.

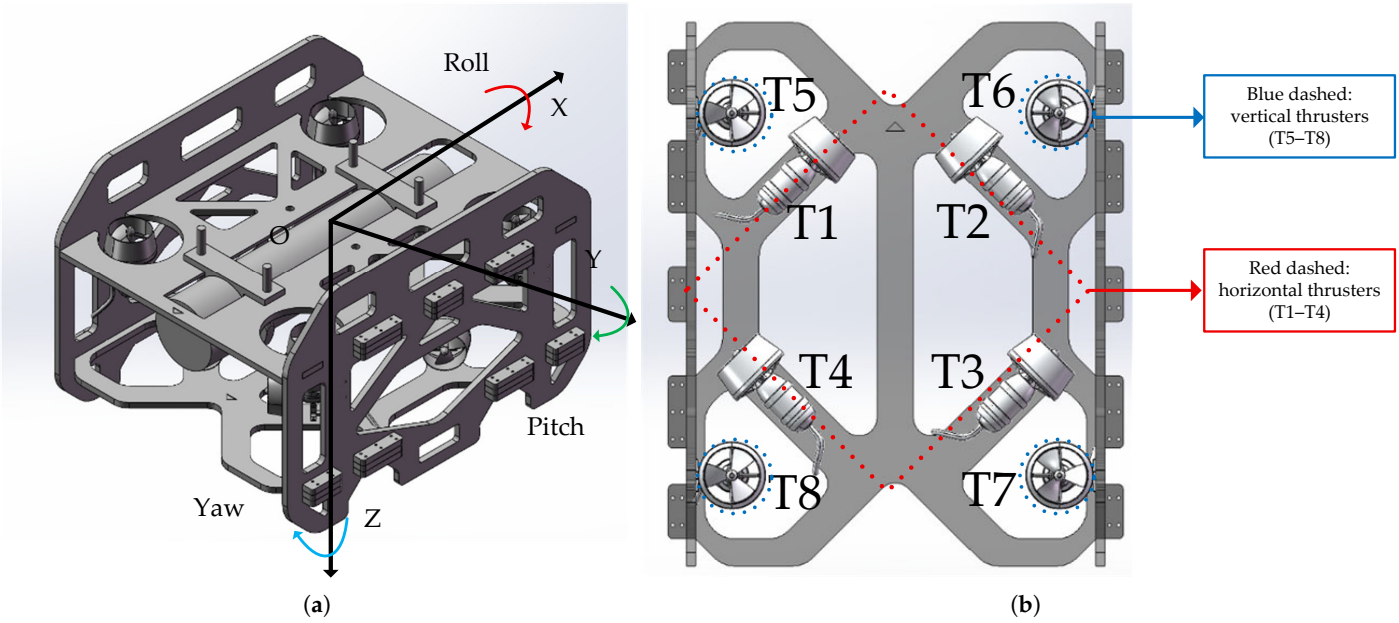

Figure 4. Thruster configuration for ROV: (**a**) 6-DOF motion; (**b**) 8-thruster layout.

Table 1. Thruster Layout Parameters of the ROV.

Index	x (mm)	y (mm)	z (mm)	Deviation Angle
T1	120	−120	130	ox axis 45°
T2	120	120	130	ox axis 45°
T3	−120	120	130	ox axis 45°
T4	−120	−120	130	ox axis 45°
T5	220	−200	0	ox axis 45°
T6	220	200	0	ox axis 45°
T7	−220	200	0	ox axis 45°
T8	−220	−200	0	ox axis 45°

The above configuration divides the thrusters into two functional groups: the horizontal thrusters (T1–T4) primarily generate surge and sway forces, as well as the yaw moment, while the vertical thrusters (T5–T8) mainly produce the heave force, roll moment, and pitch moment. The total generalized forces and moments acting on the ROV are synthesized by the combined action of all thrusters.

Let F_i $(i = 1, \ldots, 8)$ denote the thrust generated by the i-th thruster, and define the thrust vector as $\mathbf{F} = [F_1, F_2, \ldots, F_8]^T$ and the thrust command vector as $\mathbf{F}^* = [F_1^*, F_2^*, \ldots, F_8^*]^T$. The resultant body-fixed forces and moments are assembled into the generalized force vector as $\boldsymbol{\tau} = [F_x,\ F_y,\ N,\ F_z,\ K,\ M]^T$; here, F_x, F_y and F_z represent the surge, sway and heave forces, respectively, and K, M and N denote the roll, pitch and yaw moments about the body-fixed frame origin, respectively.

For the horizontal thrusters, their generated forces are first expressed in a thruster-axis-aligned coordinate frame considering the mounting angle θ. The intermediate forces and yaw moment derived from the horizontal thrusters are given by

$$\begin{bmatrix} F_{\theta x} \\ F_{\theta y} \\ N \end{bmatrix} = \mathbf{B}_h \begin{bmatrix} F_1 \\ F_2 \\ F_3 \\ F_4 \end{bmatrix}, \qquad \mathbf{B}_h = \begin{bmatrix} 0 & 1 & 0 & 1 \\ 1 & 0 & 1 & 0 \\ \alpha_z & -\alpha_z & -\alpha_z & \alpha_z \end{bmatrix} \tag{6}$$

These intermediate force components are then transformed into the body-fixed frame via the coordinate transformation matrix as follows:

$$\begin{bmatrix} F_x \\ F_y \end{bmatrix} = \mathbf{T}(\theta) \begin{bmatrix} F_{\theta x} \\ F_{\theta y} \end{bmatrix}, \qquad \mathbf{T}(\theta) = \begin{bmatrix} \sin\theta & \sin\theta \\ -\cos\theta & \cos\theta \end{bmatrix} \tag{7}$$

For the vertical thrusters, the direct mapping relationship between their thrust and the resultant body-fixed force/moment is written as

$$\begin{bmatrix} F_z \\ K \\ M \end{bmatrix} = \mathbf{B}_v \begin{bmatrix} F_5 \\ F_6 \\ F_7 \\ F_8 \end{bmatrix}, \qquad \mathbf{B}_v = \begin{bmatrix} 1 & 1 & 1 & 1 \\ -\alpha_x & \alpha_x & \alpha_x & -\alpha_x \\ -\alpha_y & -\alpha_y & \alpha_y & \alpha_y \end{bmatrix} \tag{8}$$

Here, θ denotes the mounting angle between the horizontal thruster axes and the body x-axis; $\alpha_x = l_3$, $\alpha_y = l_4$ and $\alpha_z = l_1 \sin\theta + l_2 \cos\theta$ represent the moment arms relative to the vehicle's center of mass; and l_1, l_2, l_3, l_4 are the installation distances listed in Table 1.

Based on this observation, the control-oriented thruster management framework is developed and analyzed primarily in the horizontal plane. This allows the essential characteristics of thrust allocation, actuator dynamics, coupling effects, and fault tolerance to be examined without loss of generality. The same modeling and control design procedure can be directly extended to the vertical plane by redefining the corresponding force and moment vectors, system matrices, and control objectives. Therefore, focusing on the horizontal plane in this study represents a reasonable simplification that preserves the generality of the proposed method while reducing unnecessary notational and computational complexity.

3.2. Thruster Feedback System Design

In over-actuated ROV propulsion systems, multiple thrusters jointly contribute to force and moment generation across all degrees of freedom. This configuration inherently introduces strong coupling effects, where a single thruster may influence multiple motion axes and multiple thrusters may simultaneously affect a single degree of freedom. Under such conditions, designing independent single-input single-output controllers often leads to cross-axis interference and degraded overall performance.

From a control-oriented perspective, the propulsion system can be regarded as a multi-input multi-output (MIMO) system with uncertain actuator dynamics. Thruster performance variations, parameter uncertainties, and potential faults further complicate the control problem. Instead of relying on explicit fault detection or reallocation strategies, this work aims to achieve inherent fault tolerance through feedback regulation by integrating thruster dynamics into the control loop. The framework for feedback system design is shown in Figure 5:

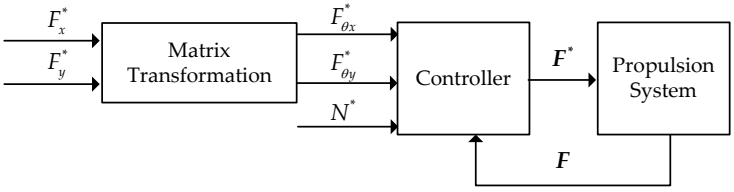

Figure 5. Over-actuated ROV thrust-torque feedback control architecture.

Using a conventional Single-Input Single-Output (SISO) controller design may be subject to interference from other control objectives. For example, in the case of torque control, the coupling situation is shown in Figure 6:

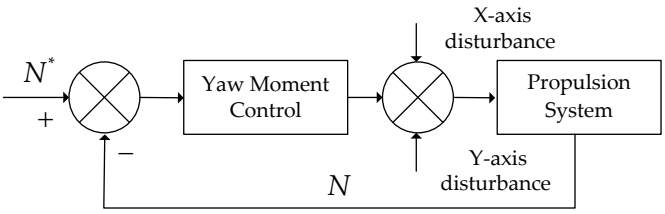

Figure 6. Control coupling in the propulsion system.

The coupling in the propulsion system arises from input coupling, where multiple thrusters control a single degree of freedom, and a single thruster may affect multiple degrees of freedom. Designing independent controllers for each degree of freedom can lead to interactions during actual thrust/torque responses. LQI control can balance system sensitivity and stability by tuning **Q** and **R** values, making it effective for multivariable systems. However, if model parameters are uncertain, the feedback coefficients calculated by LQI may mismatch the system, causing significant discrepancies in thruster response parameters. Therefore, when designing a six-degree-of-freedom controller using LQI, it is necessary to determine the thrust response model parameters of individual thrusters. As analyzed in Section 2, the thrust response of thrusters can be categorized into torque mode or speed mode, and the thrust response parameters are influenced by motor parameters, load, and controller settings. To facilitate the system-level LQI formulation, the thrust response is expressed in an equivalent form by explicitly separating the nominal dynamics and the uncertainty/disturbance terms [33]. This modeling strategy follows the common disturbance-lumping philosophy widely adopted in disturbance observer (DOB) and active disturbance rejection control (ADRC) frameworks, where parameter uncertainties and unmodeled dynamics are aggregated into an equivalent disturbance for estimation and compensation.

Accordingly, the thrust dynamics of each thruster is rewritten as

$$\begin{cases} \dot{F}_i = \dfrac{1}{T_w + \Delta T_w^i} F_i^* - \dfrac{1}{T_w + \Delta T_w^i} F_i = \dfrac{1}{T_w} F_i^* - \dfrac{1}{T_w} F_i + \Delta_w^i \\ \Delta_w^i = \left(\dfrac{1}{T_w + \Delta T_w^i} - \dfrac{1}{T_w} \right) (F_i^* - F_i) \end{cases} \tag{9}$$

where F_i is the actual thrust of the i-th thruster, F_i^* is its commanded thrust, T_w denotes the nominal thrust time constant, ΔT_w^i is the time constant uncertainty of the i-th thruster, and Δ_w^i represents the aggregated disturbance induced by the thrust dynamic model uncertainties.

Taking the horizontal plane as an example, the differential equations relating to the thrust and resultant moment of the ROV in the horizontal plane are derived on the basis of Equation (9), as given by

$$\dot{\mathbf{H}} = \mathbf{AH} + \mathbf{BF}_h^* + \mathbf{D}(\mathbf{F}_h^* - \mathbf{F}_h) \tag{10}$$

where the state matrix **A**, control matrix **B** and disturbance matrix **D** are defined as follows:

$$\mathbf{A} = -\frac{1}{T_w}\mathbf{I}_3, \quad \mathbf{B} = \begin{bmatrix} 0 & \frac{1}{T_w} & 0 & \frac{1}{T_w} \\ \frac{1}{T_w} & 0 & \frac{1}{T_w} & 0 \\ \frac{\alpha_z}{T_w} & -\frac{\alpha_z}{T_w} & -\frac{\alpha_z}{T_w} & \frac{\alpha_z}{T_w} \end{bmatrix}, \quad \mathbf{D} = \begin{bmatrix} -\frac{\Delta T_w^1}{(T_w + \Delta T_w^1)T_w} \\ -\frac{\Delta T_w^2}{(T_w + \Delta T_w^2)T_w} \\ -\frac{\Delta T_w^3}{(T_w + \Delta T_w^3)T_w} \\ -\frac{\Delta T_w^4}{(T_w + \Delta T_w^4)T_w} \end{bmatrix} \tag{11}$$

and $\mathbf{H} = [F_{\theta x},\ F_{\theta y},\ N]^{\mathrm{T}}$ denotes the vector of generalized forces and yaw moment in the thruster-axis-aligned coordinate frame for the horizontal plane, with $\mathbf{F}_h^* = [F_1^*, F_2^*, F_3^*, F_4^*]^{\mathrm{T}}$ and $\mathbf{F}_h = [F_1, F_2, F_3, F_4]^{\mathrm{T}}$ being the commanded and actual thrust vectors of the horizontal thrusters, respectively.

In Equation (10), the term $\mathbf{D}(\mathbf{F}^* - \mathbf{F})$ represents the lumped disturbance induced by the thrust dynamic uncertainties of individual thrusters. The greater the discrepancy in the time-constant uncertainties among the horizontal thrusters, the more significant this lumped disturbance becomes. It is noted that if all thrusters exhibit identical and well-matched dynamic characteristics, the propulsion system would naturally possess response consistency, and the use of an observer-based compensation would be unnecessary. However, the objective of this work is not limited to a specific, well-calibrated propulsion configuration, but rather to develop a control-oriented thrust management framework that remains applicable across different platforms and operating conditions. In practical ROV systems, achieving perfectly matched thruster dynamics typically requires extensive per-thruster tuning, such as individual adjustment of inner current loops, speed loops, or gain scheduling, and may further depend on thruster model variations, aging effects, and installation differences. By introducing an ESO to estimate and compensate the aggregated disturbance arising from these factors, the proposed framework avoids thruster-specific retuning and enhances its generality and portability, making it more suitable for practical deployment in heterogeneous propulsion systems [25]. Therefore, an ESO for individual thruster thrust response is needed to compensate for the disturbance term in Equation (9), as follows:

$$\begin{cases} e_{\hat{f}}^i = F_i - \hat{F}_i \\ \dot{\hat{\Delta}}_w^i = \beta_2 e_{\hat{f}}^i \\ \dot{\hat{F}}_i = \frac{1}{T_w} F_i^* + \hat{\Delta}_w^i + \beta_1 e_{\hat{f}}^i \end{cases} \tag{12}$$

where $e_{\hat{f}}^i$ is the estimated thrust error, $\hat{F}_i$ is the estimated thrust, $\hat{\Delta}_{w,i}$ is the disturbance estimate, and β_1, β_2 are ESO gains. The convergence of the associated ESO assumes that this equivalent disturbance evolves slowly, namely, $|\dot{\Delta}_w^i| \leq \varepsilon_2$, with ε_2 denoting a bounded constant, under which the corresponding ESO is stable and the estimation error remains bounded. The form of the designed thrust controller is shown as follows:

$$\begin{cases} e_f^i = F_i^* - F_i \\ u_f^i = k_p^f e_f^i - T_w \hat{\Delta}_w^i \end{cases} \tag{13}$$

where e_f^i denotes the thrust tracking error; u_f^i is the thrust control input; and k_p^f is the proportional gain. The control block diagram is shown in Figure 7:

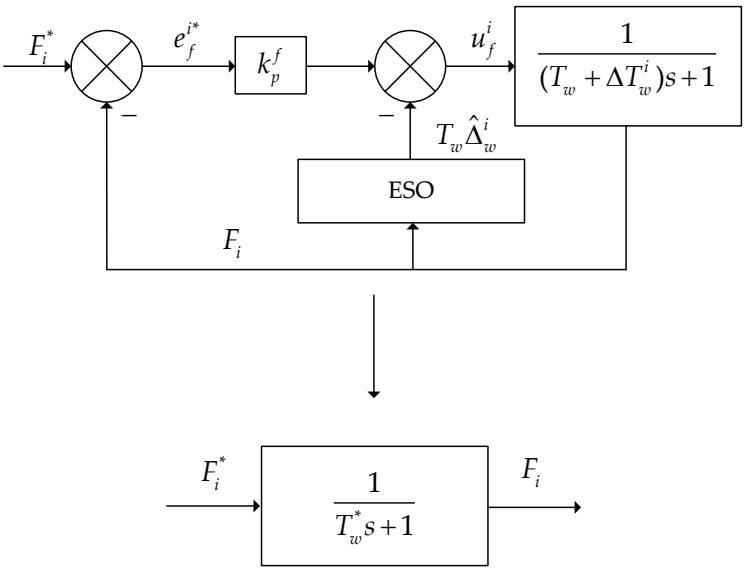

Figure 7. ESO-based thrust compensation architecture per thruster.

Regarding the tuning of the ESO parameters for thrust response compensation, it is noted that the observer bandwidth involves an inherent trade-off between responsiveness and robustness. Higher ESO gains improve disturbance estimation speed and sensitivity, which is beneficial for compensating thrust response discrepancies; however, excessively large gains amplify measurement noise and may introduce oscillations or degrade closed-loop stability. Conversely, lower ESO gains enhance noise robustness and stability margins but result in slower disturbance estimation and reduced compensation effectiveness. In practice, the ESO gains are commonly selected using pole placement or bandwidth-based tuning strategies, where the observer dynamics are shaped as a second-order system by specifying the desired natural frequency and damping ratio. Such tuning approaches are well established in the ESO and disturbance-observer literature and are therefore not repeated here. In this work, the ESO gains are selected to balance estimation responsiveness and noise sensitivity, ensuring stable operation while providing sufficient disturbance compensation within the bandwidth of the thrust dynamics.

By utilizing ESO, the thruster's inertial constant consistency is achieved, and an integral term is incorporated. Introducing an integral term, namely designing a LQI controller, can eliminate the system's steady-state error. The augmented form is presented as follows:

$$\dot{\mathbf{H}}_{\text{ext}} = \mathbf{A}_{\text{ext}}\mathbf{H}_{\text{ext}} + \mathbf{B}_{\text{ext}}\mathbf{F}_h^* + \mathbf{E}_{\text{ext}}[\mathbf{0}_{3*1}, \mathbf{H}^*]^{\text{T}} \tag{14}$$

where $\mathbf{H}_{\text{ext}}$ is the augmented state vector including integral states, $\mathbf{H}^* = [F_{\theta x}^*,\ F_{\theta y}^*,\ N^*]^{\text{T}}$ is the horizontal command vector, and the matrix $\mathbf{A}_{\text{ext}}$, $\mathbf{B}_{\text{ext}}$ and $\mathbf{E}_{\text{ext}}$ are defined as follows:

$$\begin{cases} \mathbf{A}_{\text{ext}} = \begin{bmatrix} \mathbf{A} & \mathbf{0}_{3*3} \\ -\mathbf{I}_3 & \mathbf{0}_{3*3} \end{bmatrix}, \mathbf{B}_{\text{ext}} = \begin{bmatrix} \mathbf{B} \\ \mathbf{0}_{3*4} \end{bmatrix} \\ \mathbf{E}_{\text{ext}} = \begin{bmatrix} \mathbf{0}_{3*1} \\ \mathbf{1}_{3*1} \end{bmatrix}, \mathbf{H}_{\text{ext}} = \begin{bmatrix} \mathbf{H} \\ \mathbf{Z} \end{bmatrix}, \dot{\mathbf{Z}} = \mathbf{H}^* - \mathbf{H} \end{cases} \tag{15}$$

where $\mathbf{Z}$ represents the integral states.

By leveraging the LQI algorithm, the optimal state feedback coefficients are obtained in the following form [30]:

$$\min_{\mathbf{F}^* = -\mathbf{K}\mathbf{H}_{\text{ext}}} \mathbf{J}_{\text{cost}} = \frac{1}{2}\int \mathbf{f}_{\text{ext}}^{\text{T}}\mathbf{Q}\mathbf{f}_{\text{ext}} + \mathbf{F}_h^{*\text{T}}\mathbf{R}\mathbf{F}_h^* dt \tag{16}$$

Here, $\mathbf{J}_{\text{cost}}$ represents the performance function. By using the Riccati equation, the optimal feedback matrix can be obtained, as shown below:

$$\begin{cases} \mathbf{A}_{\text{ext}}^{\text{T}}\mathbf{P} + \mathbf{P}\mathbf{A}_{\text{ext}} - \mathbf{P}\mathbf{B}_{\text{ext}}^{\text{T}}\mathbf{R}^{-1}\mathbf{B}_{\text{ext}}^{\text{T}}\mathbf{P} + \mathbf{Q} = 0_{6*6} \\ \mathbf{K} = \mathbf{R}^{-1}\mathbf{B}_{\text{ext}}^{\text{T}}\mathbf{P} \end{cases} \tag{17}$$

where $\mathbf{Q}$ and $\mathbf{R}$ are weighting matrices, $\mathbf{P}$ is the Riccati solution, and $\mathbf{K}$ is the optimal feedback gain. Considering the thruster failure, matrix $\mathbf{B}_{\text{ext}}$ will mismatch. From the perspective of a single-degree-of-freedom analysis, the LQI scheme reduces to PI control and exhibits a certain degree of disturbance-rejection capability, however, owing to parameter mismatch, the resulting PI controller parameters are no longer optimal.

From a control perspective, this formulation transforms thruster allocation from a static mapping problem into a dynamic feedback regulation problem, where coupling, parameter uncertainty, and thrust degradation can be systematically compensated within the control loop.

3.3. Quantitative Performance Metrics

To objectively evaluate the proposed ESO compensation and the LQI-based thrust allocation strategy, quantitative performance indices are defined for three scenarios, namely thrust dynamic compensation (ESO), normal step tracking with coupling suppression (LQI normal), and post-fault tolerant control (LQI fault). All metrics are computed over a short data segment immediately after each step or fault trigger.

3.3.1. ESO Compensation Metrics

The effectiveness of ESO is evaluated by measuring the consistency between the actual thrust dynamics and the nominal model:

$$\begin{cases} NRMSE_{nom} = \dfrac{\|F_i - F_{nom}\|_2}{\|F_{nom}\|_2} \\ \Delta t_{63.2} = t_i^{63.2\%} - t_{nom}^{63.2\%} \\ \sigma_{ss} = \text{std}(F_i) \end{cases} \tag{18}$$

where $NRMSE_{nom}$ quantifies nominal-model matching accuracy, $\Delta t_{63.2}$ measures the time-constant deviation, σ_{ss} reflects steady-state noise, $F_{nom}(t)$ is the output of the nominal first-order reference model, $t_{63.2\%,i}$ and $t_{63.2\%,nom}$ represent the 63.2% rise time of the measured and nominal responses, respectively, σ_{ss} is the steady-state standard deviation, and $\text{std}(\cdot)$ denotes the standard deviation operator.

3.3.2. Normal Operation Metrics

During normal step commands, both tracking accuracy and coupling suppression are considered:

$$\begin{cases} E_{F_{\theta x}}^{step} = \text{RMS}(F_{\theta x} - F_{\theta x}^{*}) \\ I_{F_{\theta y}}^{step} = \max\left|F_{\theta y} - \bar{F}_{\theta y,pre}\right| \\ I_{N}^{step} = \max\left|N - \bar{N}_{pre}\right| \end{cases} \tag{19}$$

where E_{Fx}^{step} evaluates tracking performance, I_{Fy}^{step} and I_{N}^{step} represent transient coupling impacts on non-commanded degrees of freedom, $\text{RMS}(\cdot)$ denotes the root-mean-square operator, $\bar{F}_{\theta y,pre}$ and $\bar{N}_{pre}$ represent the mean values of the corresponding signals in a short time window immediately before the step input.

3.3.3. Fault-Tolerant Metrics

After thruster failure, the controller capability is assessed using

$$\begin{cases} E_{Fx}^{fault} = \mathrm{RMS}(F_{\theta x} - F_{\theta x}^{*}) \\ C_{F_{\theta y}}^{fault} = \mathrm{RMS}(F_{\theta y}) \\ C_{N}^{fault} = \mathrm{RMS}(N) \end{cases} \tag{20}$$

These indices quantify post-fault tracking capability and stability of the remaining degrees of freedom.

4. Experimental Section

The experimental studies are designed to evaluate the proposed thruster management framework under representative underwater operating conditions. The experiments are organized progressively, starting from single-thruster behavior and extending to multi-DOF system-level control and fault scenarios. This structure allows the influence of cavitation, low-speed nonlinearity, coupling effects, and thruster failures to be examined in a systematic manner. The hardware scheme is illustrated in Figure 8:

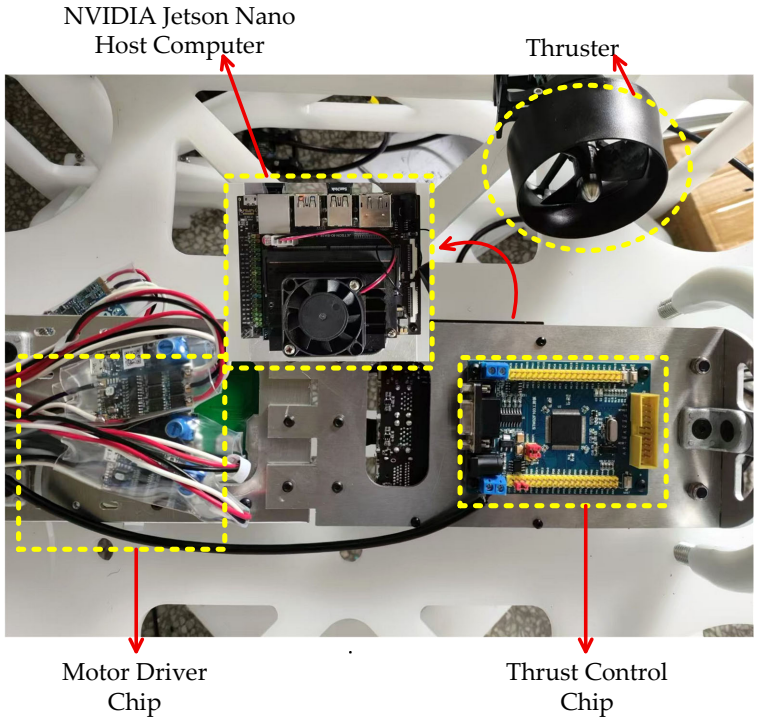

Figure 8. Hardware Scheme for Propulsion System.

The STM32F103VET6 is adopted as the main control chip, the B-G431-ESC1 as the thruster driver chip, and the Cehai Technology T60-30 thruster is employed. The parameters of the thruster are listed in Table 2.

Table 2. Electrical Parameter Table.

Parameter Name	Parameter Value
Resistance	0.413 Ω
Inductance	7.50×10^{-2} mH
Flux Linkage Constant	0.003 Wb
Moment of Inertia	2.07×10^{-6} Kg·m^2
Number of Pole Pairs	7

4.1. Cavitation Effects and Load Control

4.1.1. Load Torque Observation

Using Equation (2), a load torque observer is designed, and its parameters are selected based on a second-order observer configuration, with the natural frequency set to 200 and the damping ratio chosen as 1, namely, $\lambda_1 = 400$ and $\lambda_2 = 40,000$; the control frequency is set to 1 kHz (unless otherwise specified in subsequent experiments, this frequency is used as the default). The observation results are as shown in Figure 9:

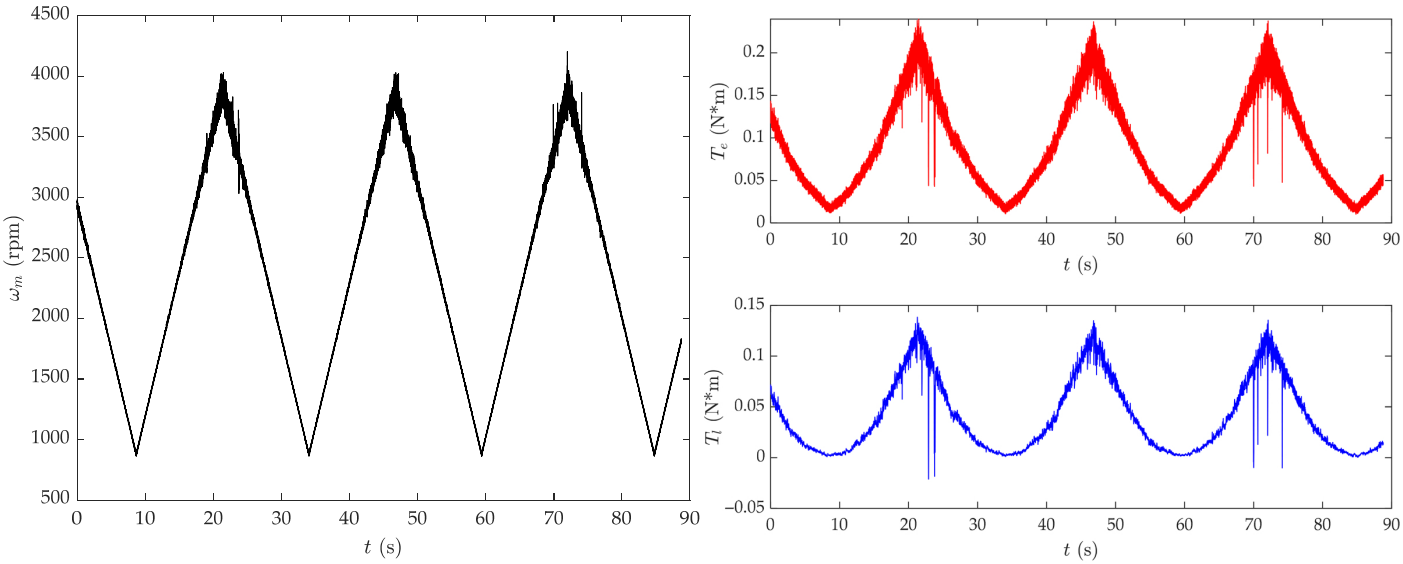

(**a**) (**b**)

Figure 9. ESO-based Load torque observation under cavitation: (**a**) measured and estimated rotor speed; (**b**) electromagnetic torque and observed load torque.

The rotational speed range of the thruster is 900 rpm to 4000 rpm. As observed in Figure 9, a cavitation-like effect occurs in the high-speed region, resulting in simultaneous pulsations of rotational speed and electromagnetic torque. At the first and third rotational speed peaks, the load torque observed by the introduced ESO indicates that the intense cavitation-like effect directly causes a sharp drop in both electromagnetic torque and load torque. At this point, the thruster loses significant thrust and thus enters a thrust oscillation state.

4.1.2. Load Torque Control

Using Equation (4), a PI controller is used to control the load torque, and its control parameters are as follows: $k_{pl} = 10,000$ and $k_{il} = 50,000$. The control results are as shown in Figure 10:

At a propeller speed of 3500 rpm, analysis of Figure 10a,b reveals two cavitation peaks that induce severe oscillations in rotor speed, electromagnetic torque, and load torque. In Figure 10a, where load torque feedback is not implemented, the rotor speed remains generally stable, except during the periods impacted by the cavitation peaks. However, due to air gap effects, the periods impacted by the cavitation peaks exhibit significant fluctuations. In contrast, Figure 10b incorporates a feedback mechanism, thereby ensuring the overall stability of the electromagnetic and load torques. Even when cavitation peak impacts occur, the system can promptly adjust the rotor speed to maintain load torque stability.

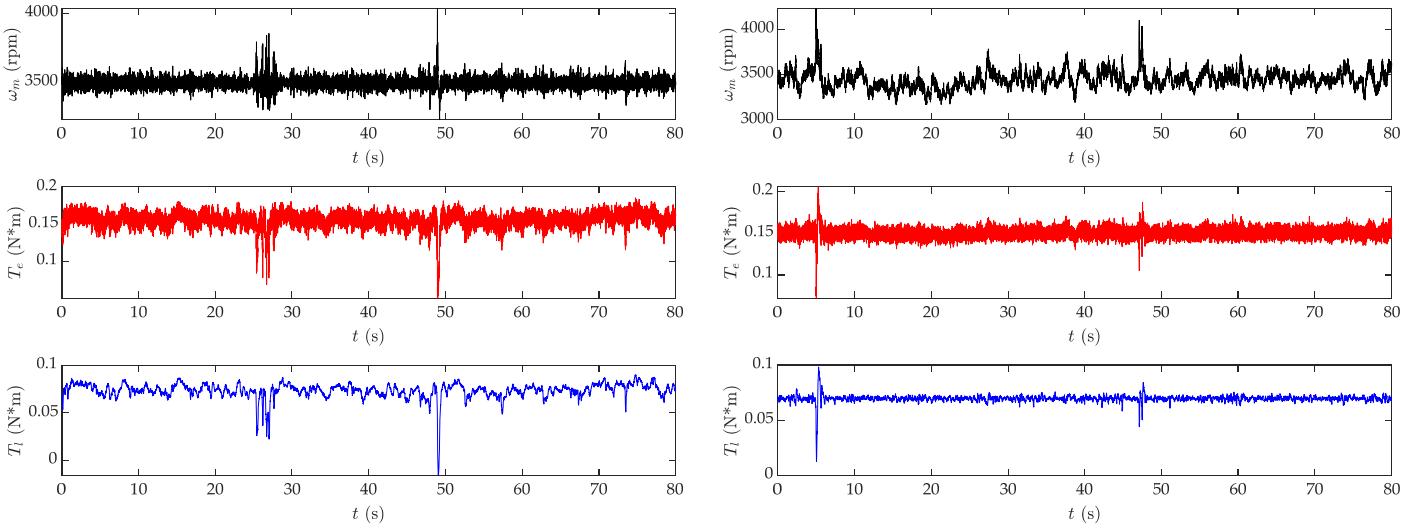

(**a**) (**b**)

Figure 10. Thruster control performance under cavitation: (**a**) speed control without load torque feedback; (**b**) load torque control with ESO-based compensation.

At low rotational speeds where cavitation does not occur, the results are as shown in Figure 11:

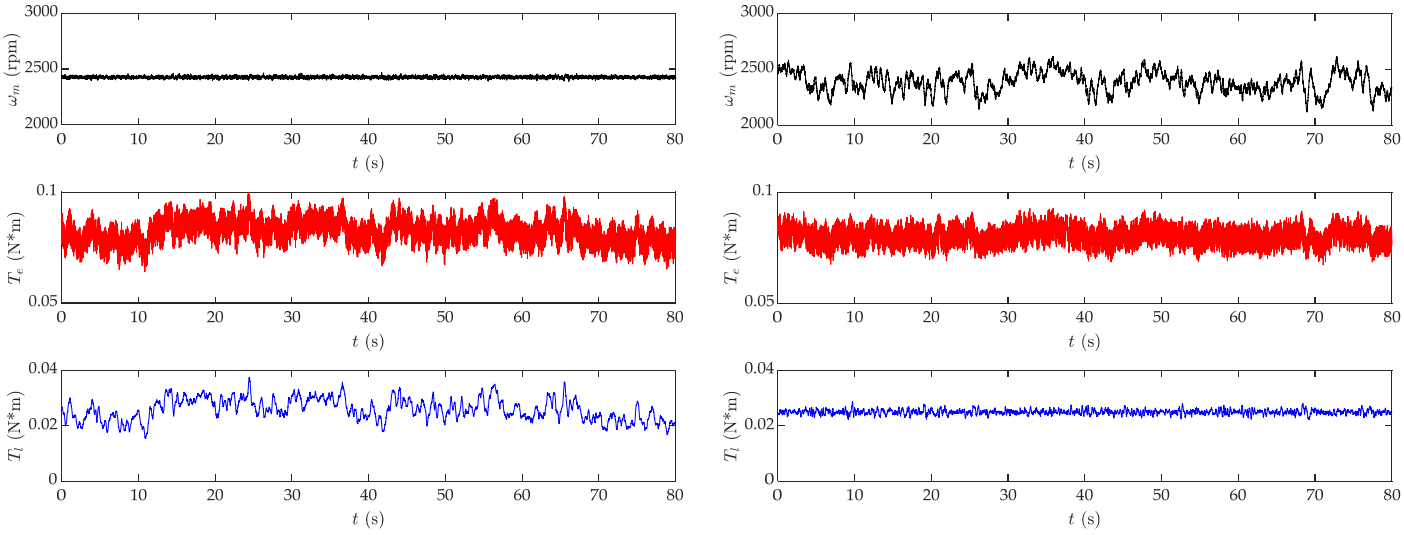

(**a**) (**b**)

Figure 11. Thruster control performance without cavitation: (**a**) speed-controlled mode; (**b**) load-torque-controlled mode.

Analyzing Figure 11a,b: at low rotational speeds where cavitation does not occur, when rotational speed is controlled, load fluctuation is observed; when the load is controlled, rotational speed fluctuation is observed.

4.2. Active Damping Control by Injecting D-Axis Current

When no current is injected, the rotational speed dead zone of the thruster is around 400 rpm, and the experimental results are shown in Figure 12:

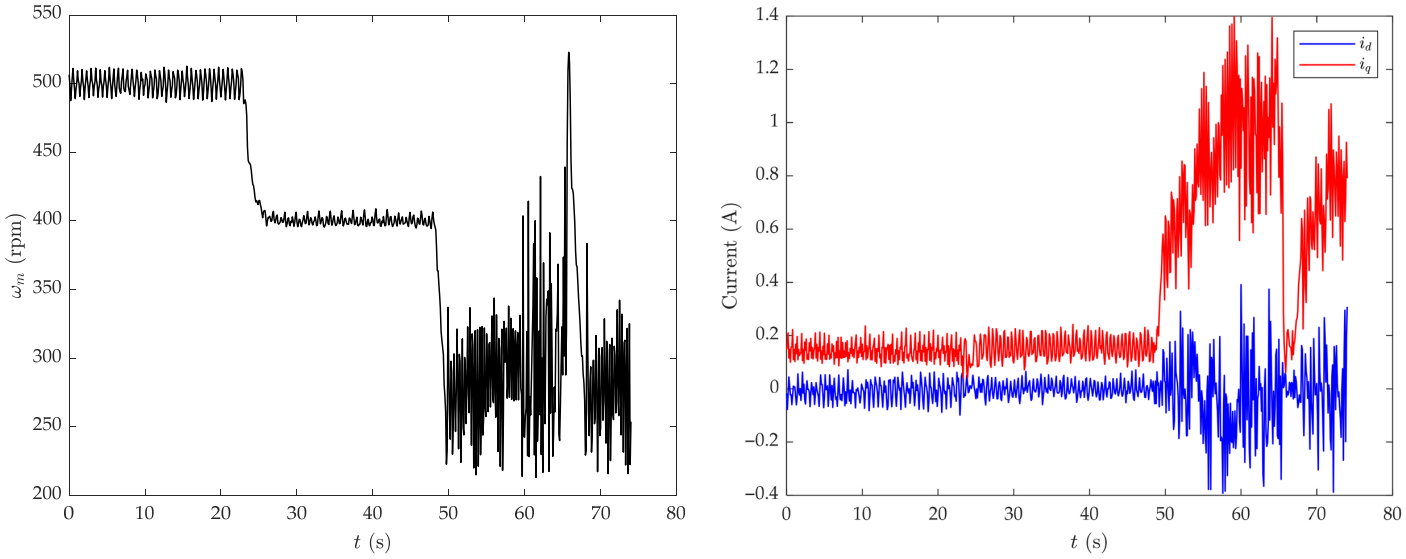

(**a**) (**b**)

Figure 12. Low-speed performance without d-axis current injection: (**a**) rotor speed; (**b**) d-axis and q-axis current.

Using Equation (5), after injecting 0.5 A of current into the d-axis, the experimental results are as shown in Figure 13:

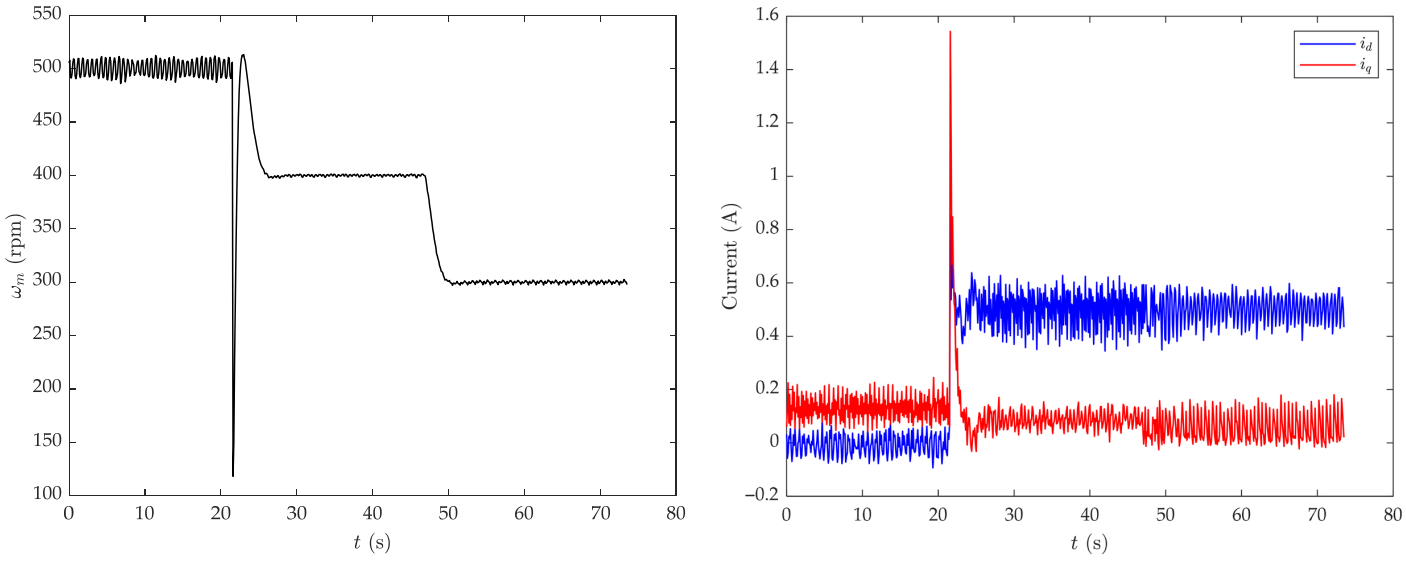

(**a**) (**b**)

Figure 13. Low-speed performance with d-axis current injection: (**a**) rotor speed; (**b**) d-axis and q-axis current.

In the aforementioned experiments, when the rotational speed is below 500 rpm, 0.5 A of current is injected into the d-axis. The thruster exhibits a certain degree of speed ripple initially, after which the rotational speed converges stably. Even when the speed command is 300 rpm (within the original dead zone), the thruster still maintains a steady state.

At low rotational speeds, the performance of current injection is as shown in Figure 14:

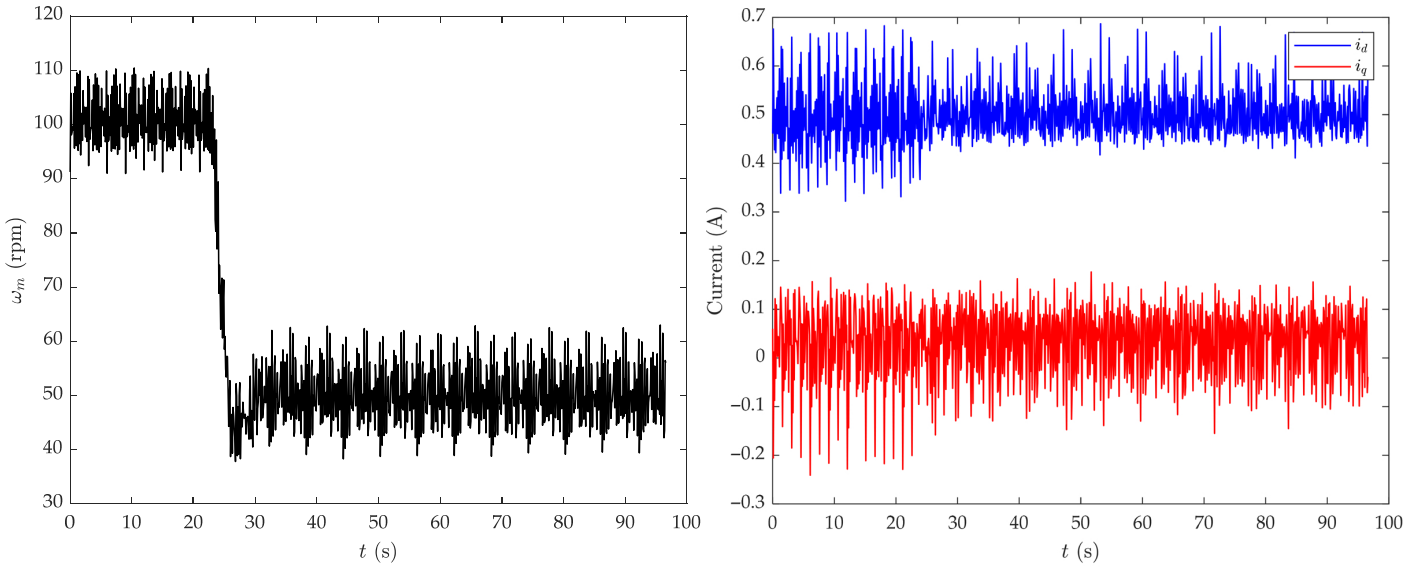

(**a**) (**b**)

Figure 14. Ultra-low-speed with d-axis current injection: (**a**) speed tracking at 50–100 rpm; (**b**) corresponding current responses.

During the process of the speed command changing from 100 rpm to 50 rpm, the thruster can maintain stability, with the rotational speed fluctuating around 10 rpm.

4.3. LQI-ESO Control

First, the compensation effect of the ESO is evaluated. After introducing the ESO, the response of the actual model will approach the nominal model; in this experiment, the nominal model is set as $G_n(s) = \frac{1}{0.25s+1}$. The control frequency is set at 100 Hz. Using Equations (12) and (13), the ESO parameters are selected based on a second-order observer configuration, with the natural frequency set to 10 and the damping ratio chosen as 1, namely, $\beta_1 = 20$ and $\beta_2 = 100$. This conservative tuning ensures stable disturbance estimation while avoiding excessive noise amplification in practical experiments. When the speed loop gain $k_{p\omega} = 0.0001$, its thrust response is close to that of the nominal model. Under this condition, with the addition of ESO compensation, the model results are as shown in Figure 15.

The direct response is basically consistent with the ESO-compensated response and close to the nominal model.

When the speed loop gain $k_{p\omega} = 0.00005$, the results of the direct response and the ESO-compensated model are as shown in Figure 16.

The direct response lags behind the nominal model, while the ESO-compensated model can compensate for the deviation and approximate the nominal model.

When the speed loop gain $k_{p\omega} = 0.0002$, the results of the direct response and the ESO-compensated model are as shown in Figure 17.

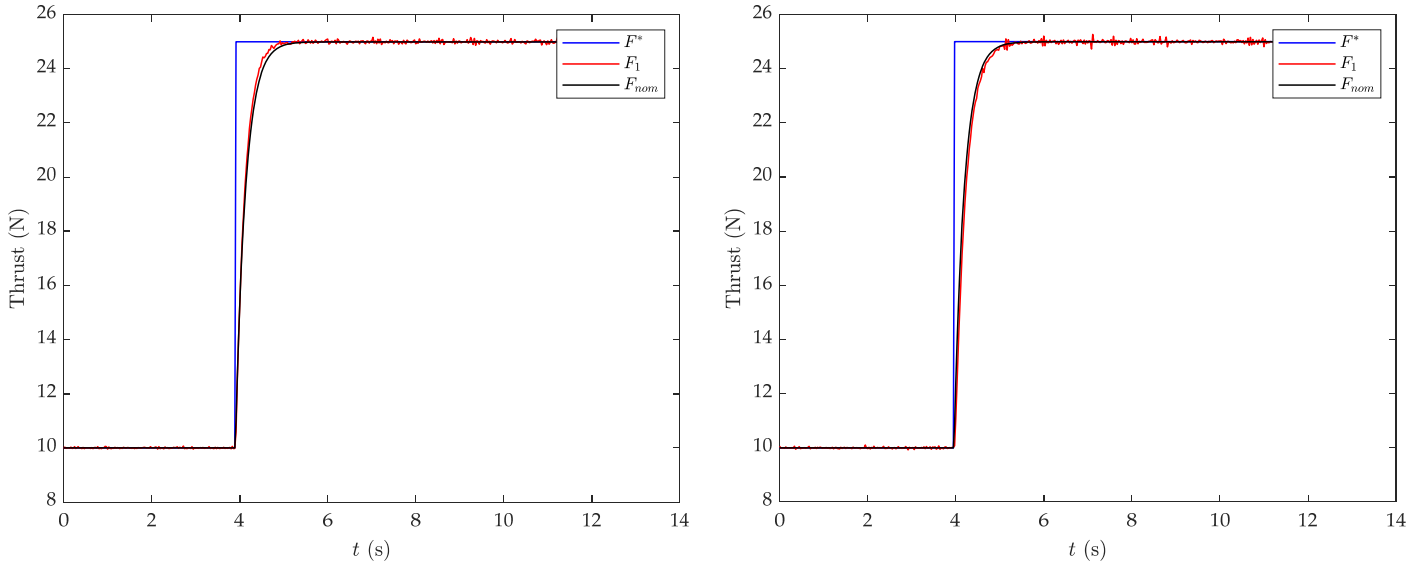

(**a**) (**b**)

Figure 15. Thrust response comparison with and without ESO compensation ($k_{p\omega} = 0.0001$): (**a**) direct thrust response; (**b**) ESO-compensated response.

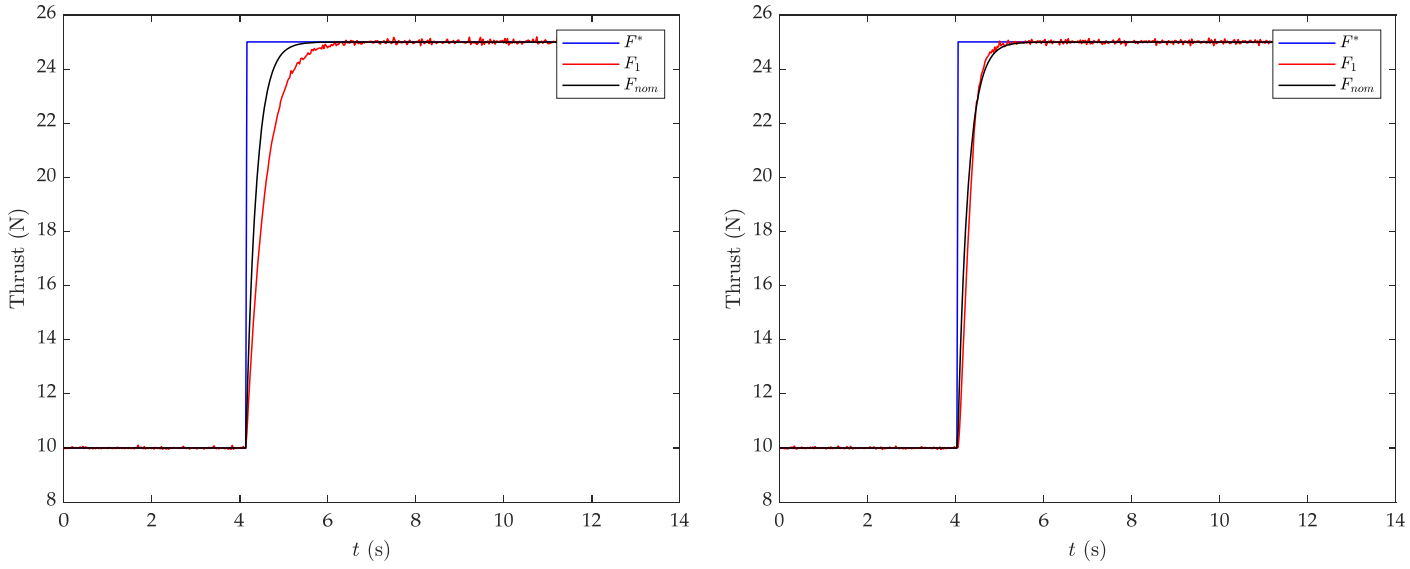

(**a**) (**b**)

Figure 16. Thrust response comparison with and without ESO compensation ($k_{p\omega} = 0.00005$): (**a**) direct thrust response; (**b**) ESO-compensated response.

The direct response leads the nominal model, while the ESO-compensated model can still compensate for the deviation and approximate the nominal model. However, after entering the steady state, a certain degree of noise is introduced. To quantitatively evaluate the effectiveness of ESO compensation under different speed-loop gains, Table 3 summarizes the normalized tracking performance of both direct and ESO-compensated responses, where the performance index reflects the closeness to the nominal model.

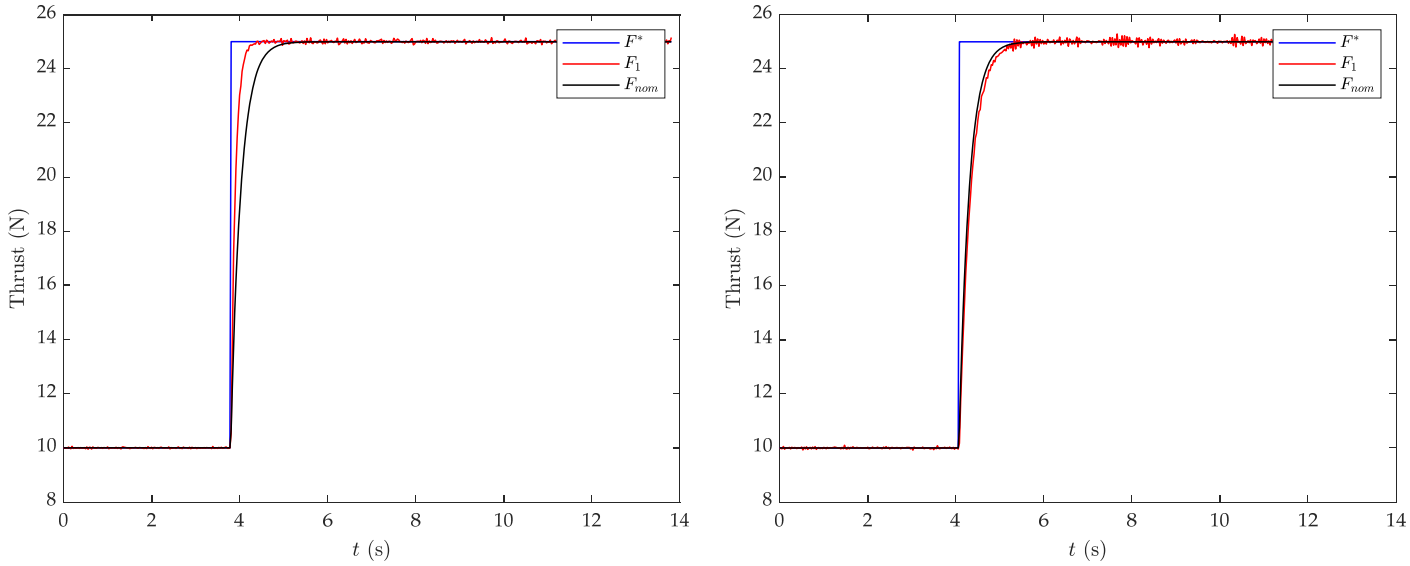

(**a**) (**b**)

Figure 17. Thrust response comparison with and without ESO compensation ($k_{p\omega} = 0.0002$): (**a**) direct thrust response; (**b**) ESO-compensated response.

Table 3. ESO Compensation Performance with Quantitative Indices.

$k_{p\omega}$	Method	$NRMSE_{nom} \downarrow$	$\Delta t_{63.2}$ (s) $\downarrow$	$\sigma_{ss} \downarrow$
0.00010	Direct	0.0161	0.0000	2.7624
	ESO	0.0329	0.0556	3.2178
0.00020	Direct	0.1095	−0.1111	1.8574
	ESO	0.0279	0.0556	3.1081
0.00005	Direct	0.1222	0.1944	3.5618
	ESO	0.0554	0.0833	3.5962

As shown in Table 3, ESO improves the consistency between the actual thrust and the nominal model. In particular, when $k_{p\omega} = 2 \times 10^{-4}$, the nominal mismatch $NRMSE_{nom}$ is significantly reduced. Meanwhile, the time constant deviation becomes more stable, indicating improved dynamic behavior. A slight increase in σ_{ss} is observed due to bandwidth enhancement, revealing the expected noise–performance trade-off.

Using Equations (16) and (17), two sets of parameters are designed to compare the performance of the LQI controller, as shown in Figure 18:

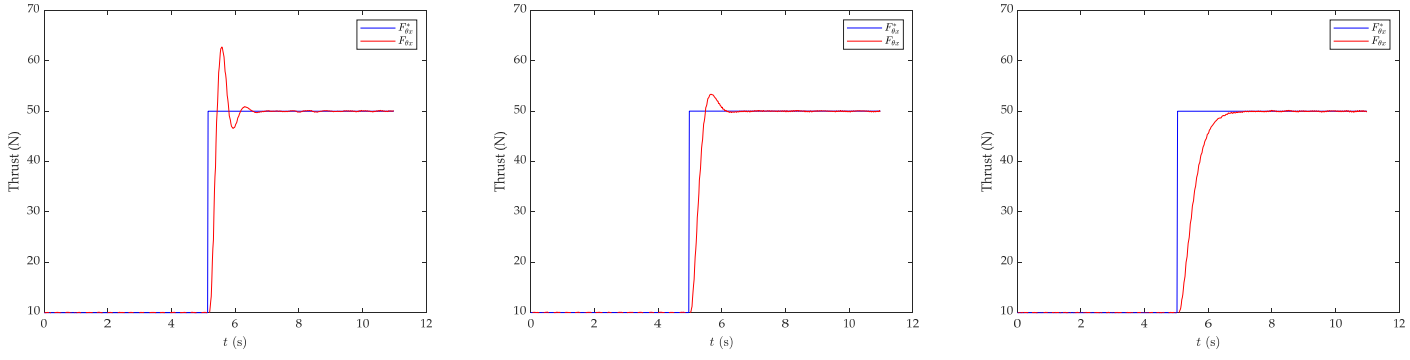

(**a**) (**b**) (**c**)

Figure 18. *Cont.*

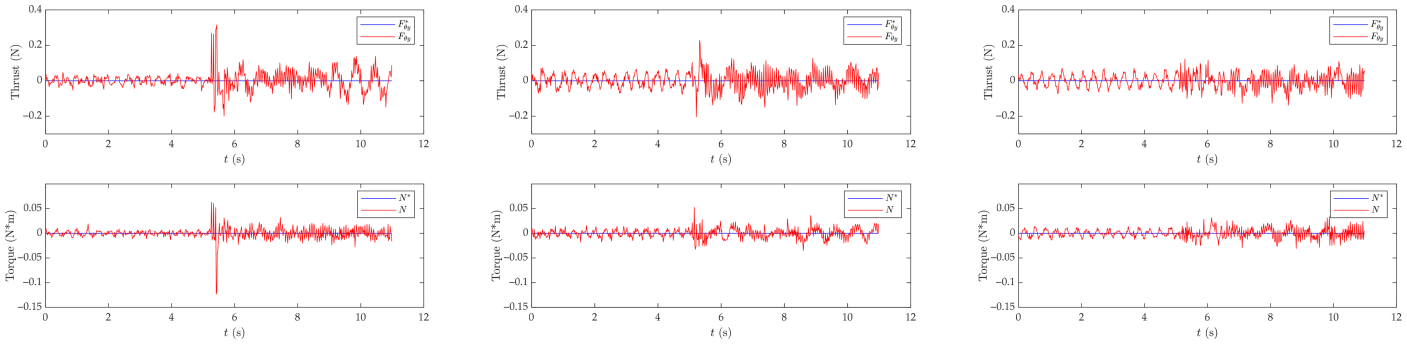

(**d**) (**e**) (**f**)

Figure 18. Thrust and torque responses under different LQI weighting matrices ($\mathbf{Q} = \mathbf{100I_3}$): (**a**–**c**) F_x responses with $\mathbf{R} = \mathbf{5I_4}$, $\mathbf{R} = \mathbf{25I_4}$, and $\mathbf{R} = \mathbf{125I_4}$; (**d**–**f**) corresponding F_y and yaw moment responses.

To further analyze the trade-off between response speed and coupling suppression, Table 4 qualitatively summarizes the system behavior under different LQI damping coefficients.

Table 4. LQI Response and Interference Suppression under Different Damping Coefficients.

R	$RMS(F_x - F_{x,ref}) \downarrow$	$I_{Fy} \downarrow$	$I_N \downarrow$
5	11.8818	0.3175	0.1225
25	13.0916	0.2267	0.0511
125	16.8178	0.1219	0.0317

The comparison results with direct allocation are as shown in Figure 19:

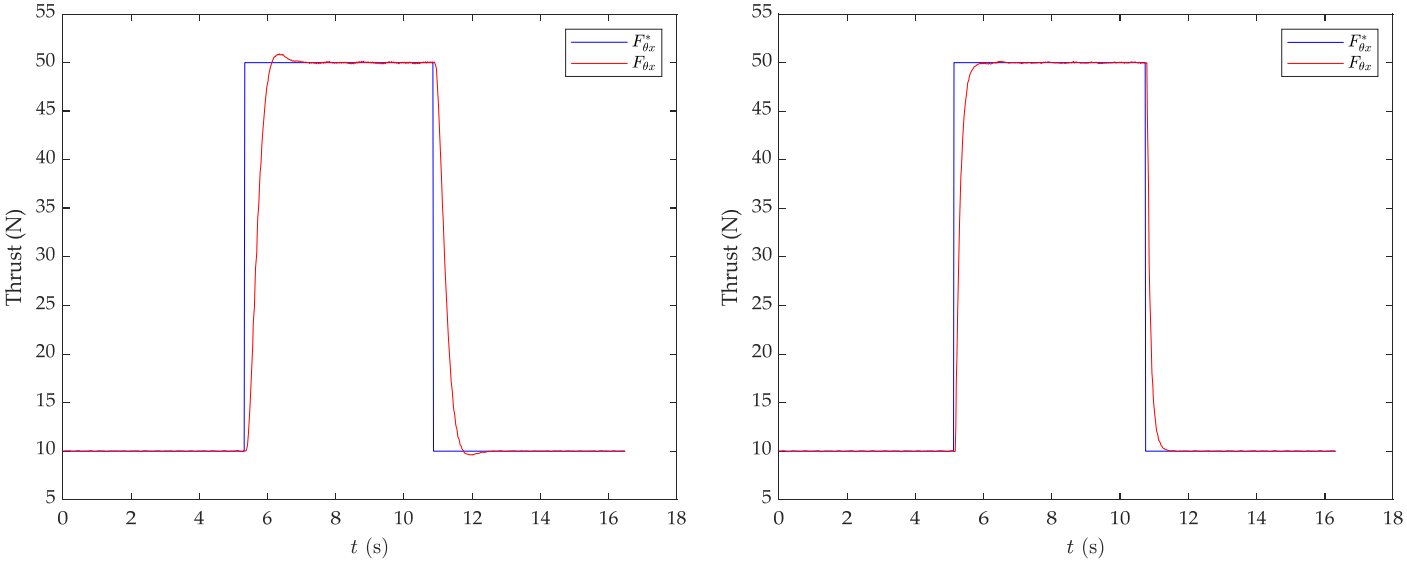

(**a**) (**b**)

Figure 19. Comparison between LQI control and direct allocation for surge force tracking (F_x): (**a**) LQI-based control; (**b**) direct thrust allocation.

For the F_x, the introduction of LQI control results in slight delays and overshoot in the overall control performance. The direct allocation acts as a feedforward term and

outperforms LQI control under the single-DOF condition. However, the propulsion system is a coupled system. For the F_y and N cases, the results are as shown in Figure 20:

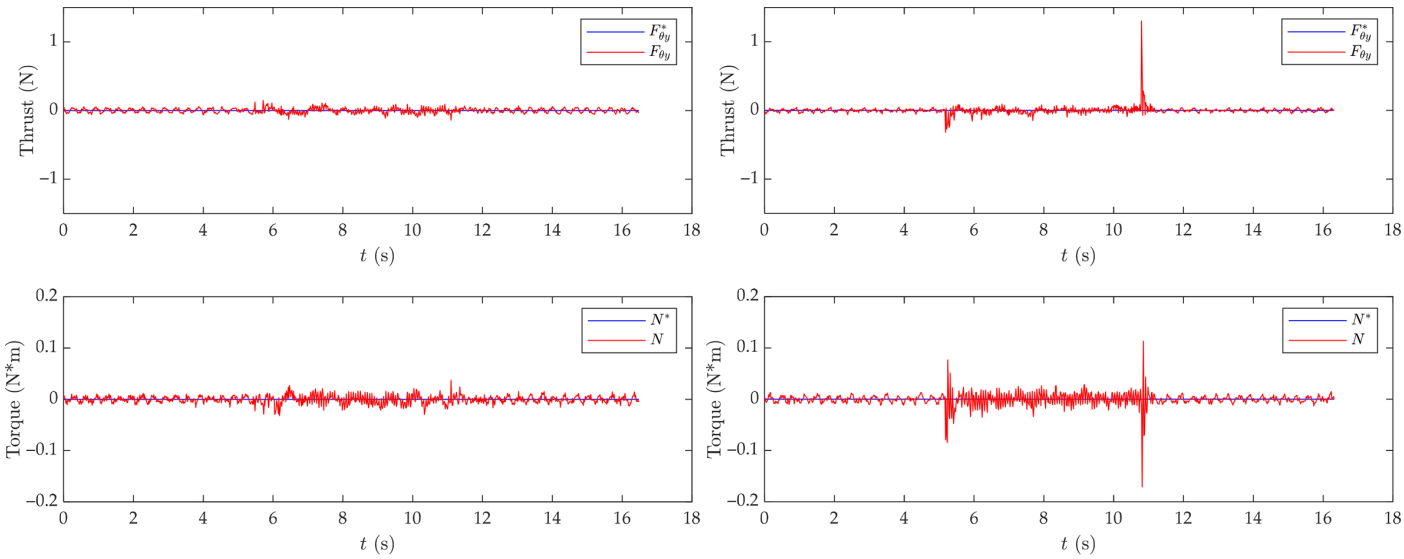

(**a**) (**b**)

Figure 20. Comparison between LQI control and direct allocation under coupled conditions: (**a**) F_y and yaw moment responses using LQI control; (**b**) responses using direct allocation.

Under the allocation strategy, the F_y and N are disturbed by the F_x, while the LQI control can suppress the interference to a great extent. The data analysis is shown in the following Table 5:

Table 5. LQI Normal-Operation Performance under Step Commands.

Edge	Strategy	$RMS(F_x - F_{x,ref}) \downarrow$	$I_{Fy} \downarrow$	$I_N \downarrow$
Up	LQI	14.6511	0.1401	0.0344
	Direct	9.7208	0.3199	0.0849
Down	LQI	14.4151	0.1424	0.0378
	Direct	8.7195	1.2924	0.1735

Table 5 reports the normal-operation performance under step commands.

The experimental results of fault-tolerant control are as shown in Figure 21.

In the fault-tolerant control experiment, after the propulsion system operates stably for a period of time, the T1 thruster is shut down. At this point, the system remains in a controllable state. However, since the direct allocation strategy lacks fault-tolerant capability, the system fails to track the command, and all degrees of freedom are affected. In contrast, the LQI control can continue to track the command through feedback adjustment. For the F_y and N cases, the results are as shown in Figure 22.

To summarize the fault-tolerant behavior under thruster failure in a concise manner, Table 6 compares the system-level responses of different control strategies.

Table 6 evaluates the post-fault behavior. After thruster failure, the direct allocation rapidly loses controllability, resulting in large tracking errors and strong oscillations.

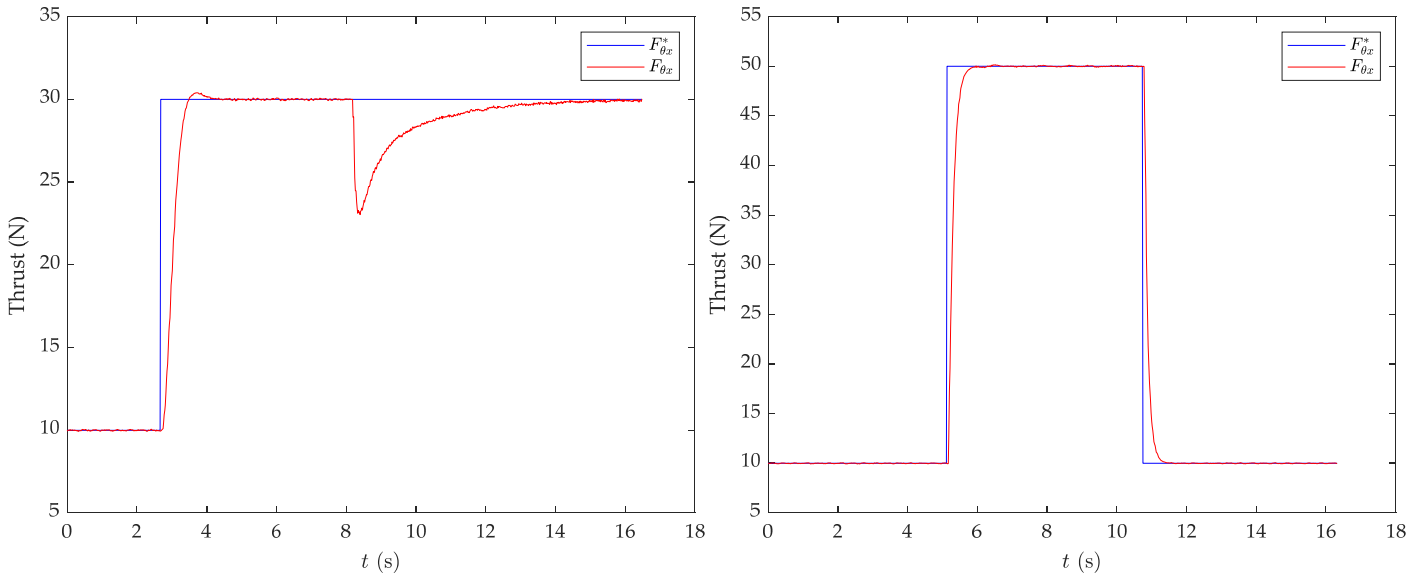

(**a**) (**b**)

Figure 21. Fault-tolerant performance under T1 thruster failure: (**a**) F_x response using LQI control; (**b**) F_x response using direct allocation.

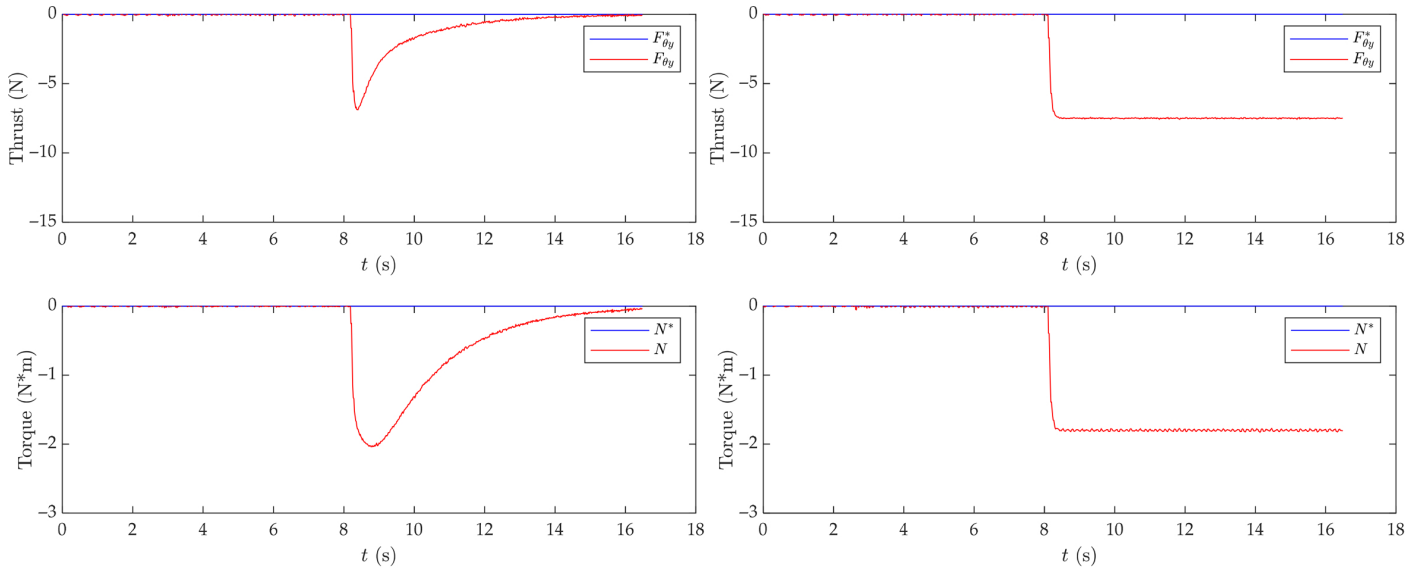

(**a**) (**b**)

Figure 22. Coupled DOF responses under T1 thruster failure: (**a**) F_y and yaw moment responses using LQI control; (**b**) responses using direct allocation.

Table 6. LQI Fault-Tolerant Performance.

Strategy	$RMS(F_x - F_{x,ref}) \downarrow$	$RMS(F_y) \downarrow$	$RMS(N) \downarrow$
LQI	1.9789	1.9756	0.9501
Direct	7.4437	7.4431	1.7861

5. Discussion

This section provides a consolidated interpretation of the experimental observations reported in Section 4. Rather than repeating the numerical results, the discussion focuses

on clarifying how the measured behaviors reflect the effectiveness and limitations of the proposed control-oriented thruster management framework.

5.1. Cavitation Compensation at the Actuator Level

The load torque observation results in Figure 9 demonstrate that cavitation at high rotational speeds introduces simultaneous pulsations in rotor speed, electromagnetic torque, and load torque. The ESO-estimated load torque closely follows these rapid variations, indicating that the observer can capture the dominant disturbance dynamics.

As shown in Figures 10 and 11, after introducing load torque control, load torque stability is maintained at the expense of rotor speed stability, thereby preserving thrust stability. However, under the influence of external interference, the system cannot generally maintain stable operation. Meanwhile, under shallow water conditions, rotor speed stability and load torque stability cannot be achieved simultaneously. Pursuing rotor speed stability necessitates sacrificing load torque stability, and conversely, pursuing load torque stability requires sacrificing rotor speed stability.

These results confirm that the proposed load-torque-based control effectively suppresses cavitation-induced thrust fluctuations, thereby providing a stable and reliable thrust response for higher-level control.

5.2. Low-Speed Dead-Zone Mitigation via D-Axis Injection

The low-speed experiments further reveal a clear dead-zone phenomenon when no d-axis current is injected. As shown in Figure 12, the thruster stalls or exhibits severe chattering when the command is below approximately 400 rpm, accompanied by large current spikes.

After injecting 0.5 A on the d-axis, Figure 13 shows that the rotor speed converges to a stable value even for commands within the original dead-zone region. At ultra-low speeds (50–100 rpm), Figure 14 demonstrates that the thruster remains controllable with limited speed fluctuation.

These results indicate that d-axis current injection effectively restores controllability and stabilizes torque generation at low speeds. Rather than improving efficiency, the injection mainly enhances observability and damping, thereby enabling reliable small-thrust execution that is otherwise unattainable with conventional sensorless control.

5.3. ESO-Based Thrust Dynamics Equalization

The effectiveness of ESO compensation on thrust dynamics is illustrated in Figures 15–17. When the nominal response is already matched (Figure 15), ESO compensation produces little change. However, when the system exhibits lagging or leading behavior (Figures 16 and 17), the compensated responses move closer to the nominal model.

The quantitative comparison in Table 3 confirms this trend across different speed-loop gains. In all cases, the ESO reduces deviation from the nominal response, although slight steady-state noise appears at high gains.

This evidence suggests that ESO compensation improves the consistency of individual thruster dynamics, which is beneficial for higher-level coordinated control where mismatched time constants would otherwise introduce coupling disturbances.

5.4. System-Level Coupling Suppression with LQI Control

System-level experiments highlight the difference between direct allocation and feedback-based coordination. For single-DOF surge tracking, Figure 19 shows that direct allocation achieves slightly faster responses, whereas LQI introduces mild delay and overshoot. However, under coupled conditions, Figure 20 indicates that direct allocation causes significant disturbances on F_y and yaw moment N when F_x changes.

In contrast, the LQI controller substantially suppresses cross-axis interference. This behavior is quantitatively supported by Table 5, where the fluctuation and variance of F_y and N are markedly reduced.

The weighting study in Figure 18 and Table 4 further reveals the expected trade-off between response speed and damping: smaller **R** values yield faster but oscillatory responses, while larger **R** values improve decoupling and smoothness.

Overall, these results demonstrate that incorporating a MIMO feedback structure provides improved coordination and disturbance rejection compared with purely feedforward allocation.

5.5. Fault-Tolerant Characteristics

Fault scenarios in Figures 21 and 22 show that, after disabling thruster T1, direct allocation fails to maintain tracking and induces large deviations in all DOFs. By contrast, the LQI-based controller preserves stable responses and continues to track commands through feedback adjustment.

Table 6 summarizes this difference, indicating that the feedback-based strategy retains controllability without explicit fault reconfiguration.

This behavior suggests that the proposed framework achieves inherent fault tolerance by absorbing actuator loss within the closed-loop regulation, which reduces reliance on additional fault-detection or reallocation mechanisms.

5.6. Overall Implications

Across all experiments, the results consistently show that explicitly incorporating actuator dynamics into the control loop improves thrust stability, low-speed executability, coupling suppression, and robustness to failures. These properties are not simultaneously achieved by conventional speed control or direct thrust allocation, highlighting the practical benefits of the proposed control-oriented thruster management formulation.

6. Conclusions

This paper presented a control-oriented thruster management framework for ROV propulsion systems by integrating actuator-level load-torque compensation with system-level LQI coordination. The effectiveness of the proposed design is validated through comprehensive experiments at both the single-thruster and multi-thruster levels.

Quantitatively, the ESO-based load-torque regulation significantly suppresses cavitation-induced thrust fluctuations and improves dynamic consistency among thrusters, reducing the deviation from the nominal response under different speed-loop gains, as summarized in Table 3. At low speeds, the proposed d-axis current injection eliminates the dead-zone phenomenon and enables stable small-thrust generation, thereby restoring controllability in the near-zero-speed region. At the system level, the LQI controller explicitly accounts for multi-axis coupling and reduces cross-axis interference compared with direct allocation, with the interference indices markedly decreased (Table 5). Furthermore, under single-thruster fault conditions, the closed-loop strategy maintains bounded RMS tracking errors for all DOFs, whereas the open-loop allocation fails to preserve stable tracking performance (Table 6).

These improvements enhance thrust stability, low-speed maneuverability, and inherent fault tolerance, which are critical for practical ROV operations in confined, disturbance-prone, or safety-sensitive underwater environments. Compared with conventional static allocation approaches, the proposed framework provides a unified feedback solution that incorporates actuator dynamics and coupling effects into the control loop, resulting in

improved robustness, coordination, and deployment reliability for over-actuated propulsion systems.

Future work will focus on further enhancing the control-oriented framework from both actuator and system levels. In particular, we plan to investigate identification and adaptation strategies under actuator faults and model mismatch, enabling online estimation of degraded thruster dynamics to improve robustness and fault accommodation. In addition, the dynamic characteristics introduced by the LQI-based regulation, such as closed-loop lag and bandwidth limitations, will be explicitly considered in the upper-level motion control design to achieve better coordination between propulsion control and high-level trajectory tracking. These directions aim to further strengthen the adaptability and real-world applicability of the proposed framework in complex and uncertain underwater environments.

Author Contributions: Conceptualization, L.W. and Z.Z.; Methodology, L.W. and Z.Z.; Software, L.W.; Validation, L.W. and Z.Z.; Formal analysis, L.W. and Y.W.; Investigation, L.W.; Data curation, L.W. and Y.W.; Writing—original draft, L.W.; Writing—eview & editing, L.W., Y.W., C.F., J.G. and Z.Z.; Visualization, Y.W. and Z.Z.; Supervision, Y.W., C.F., Y.G. and Z.Z.; Project administration, C.Z.; Funding acquisition, Y.G. and C.Z. All authors have read and agreed to the published version of the manuscript.

Funding: This research received no external funding.

Data Availability Statement: The original contributions presented in this study are included in the article. Further inquiries can be directed to the corresponding authors.

Conflicts of Interest: The authors declare no conflicts of interest.

References

1. Ohrem, S.J.; Amundsen, H.B.; Caharija, W.; Holden, C. Robust Adaptive Backstepping DP Control of ROVs. *Control Eng. Pract.* **2022**, *127*, 105282. [CrossRef]
2. Hosseinnajad, A.; Loueipour, M. Design of a Robust Observer-Based DP Control System for an ROV with Unknown Dynamics Including Thruster Allocation. In Proceedings of the 2021 7th International Conference on Control, Instrumentation and Automation (ICCIA), Tabriz, Iran, 23–24 February 2021; pp. 1–6. [CrossRef]
3. Sørensen, A.J. A Survey of Dynamic Positioning Control Systems. *Annu. Rev. Control* **2011**, *35*, 123–136. [CrossRef]
4. Bartlett, B.; Trslic, P.; Santos, M.; Penica, M.; Riordan, J.; Dooly, G. Dynamic Positioning System for Low-Cost ROV. In Proceedings of the OCEANS 2023—Limerick, Limerick, Ireland, 5–8 June 2023; pp. 1–5. [CrossRef]
5. Hosseinnajad, A.; Loueipour, M. Fault Tolerant Control System for an ROV Based on a Novel Integral Sliding Mode Control and a State and Fault Observer in the Presence of Thruster Limitations. *Ocean Eng.* **2023**, *280*, 114687. [CrossRef]
6. Sarkar, N.; Podder, T.K.; Antonelli, G. Fault-Accommodating Thruster Force Allocation of an AUV Considering Thruster Redundancy and Saturation. *IEEE Trans. Robot. Autom.* **2002**, *18*, 223–233. [CrossRef]
7. Liu, C.; Zhang, Y.; Gu, M.; Zhang, L.; Teng, Y.; Tian, F. Experimental Study on Adaptive Backstepping Synchronous Following Control and Thrust Allocation for a Dynamic Positioning Vessel. *J. Mar. Sci. Eng.* **2024**, *12*, 203. [CrossRef]
8. Li, X.; Yang, L. Fault-Tolerant Thrust Allocation Analysis Using Metaheuristic Optimization Algorithms. *Ocean Eng.* **2024**, *299*, 117269. [CrossRef]
9. Tang, Z.; He, H.; Wang, L.; Wang, X. An Optimal Thrust Allocation Algorithm with Bivariate Thrust Efficiency Function Considering Hydrodynamic Interactions. *J. Mar. Sci. Technol.* **2022**, *27*, 52–66. [CrossRef]
10. Zalewski, P. Convex Optimization of Thrust Allocation in a Dynamic Positioning Simulation System. *Sci. J. Marit. Univ. Szczec.* **2016**, *48*, 58–62. [CrossRef]
11. Zalewski, P. Constraints in Allocation of Thrusters in a DP Simulator. *Sci. J. Marit. Univ. Szczec.* **2017**, *52*, 45–50. [CrossRef]
12. Ding, Q.; Deng, F.; Zhang, S.; Du, Z.; Yang, H. Multi-Objective Optimization for Thrust Allocation of Dynamic Positioning Ship. *J. Mar. Sci. Eng.* **2024**, *12*, 1118. [CrossRef]
13. Ji, M.; Yi, B. The Optimal Thrust Allocation Based on QPSO Algorithm for Dynamic Positioning Vessels. In Proceedings of the 2014 IEEE International Conference on Mechatronics and Automation, Tianjin, China, 3–6 August 2014; pp. 1365–1370. [CrossRef]
14. Li, M.; Yu, C.; Zhang, X.; Liu, C.; Lian, L. Fuzzy Adaptive Trajectory Tracking Control of Work-Class ROVs Considering Thruster Dynamics. *Ocean Eng.* **2023**, *267*, 113232. [CrossRef]

15. Miao, J.; Wang, S.; Zhao, Z.; Li, Y.; Tomovic, M.M. Spatial Curvilinear Path Following Control of Underactuated AUV with Multiple Uncertainties. *ISA Trans.* **2017**, *67*, 107–130. [CrossRef]
16. Hu, X.; Du, J. Robust nonlinear control design for dynamic positioning of marine vessels with thruster system dynamics. *Nonlinear Dyn.* **2018**, *94*, 365–376. [CrossRef]
17. Li, J.; Wang, D.; Wu, X.; Xu, K.; Liu, X. Vibration prediction of the robotic arm based on elastic joint dynamics modeling. *Sensors* **2022**, *22*, 6170. [CrossRef] [PubMed]
18. Luo, Y.; Tao, J.; Li, Z.; Ding, L.; Deng, Z.; Sun, H.; Song, X. An Accurate Cavitation Prediction Thruster Model Based on Gaussian Process Regression. In Proceedings of the 2017 IEEE International Conference on Robotics and Biomimetics (ROBIO), Macau, China, 5–8 December 2017; pp. 575–580. [CrossRef]
19. Xu, D.; Zhang, S.; Liu, J. Very-Low Speed Control of PMSM Based on EKF Estimation with Closed Loop Optimized Parameters. *ISA Trans.* **2013**, *52*, 835–843. [CrossRef] [PubMed]
20. Cavanini, L.; Ippoliti, G. Fault Tolerant Model Predictive Control for an Over-Actuated Vessel. *Ocean Eng.* **2018**, *160*, 1–9. [CrossRef]
21. Hosseinnajad, A.; Mohajer, N.; Nahavandi, S. Novel Barrier Lyapunov Function-Based Backstepping Fault Tolerant Control System for an ROV with Thruster Constraints. *Ocean Eng.* **2023**, *285*, 115312. [CrossRef]
22. Baldini, A.; Ciabattoni, L.; Felicetti, R.; Ferracuti, F.; Freddi, A.; Monteriù, A. Dynamic Surface Fault Tolerant Control for Underwater Remotely Operated Vehicles. *ISA Trans.* **2018**, *78*, 10–20. [CrossRef]
23. Zhong, K.; Han, M.; Han, B. Data-Driven Based Fault Prognosis for Industrial Systems: A Concise Overview. *IEEE/CAA J. Autom. Sin.* **2020**, *7*, 330–345. [CrossRef]
24. Zhou, W.; Song, Z.; Xiao, X.; Guo, Y.; Mo, Y. Sliding Mode Speed Control for PMSM Based on Model Predictive Current. *Electronics* **2024**, *13*, 2561. [CrossRef]
25. Zhu, G.; Dessaint, L.; Akhrif, O.; Kaddouri, A. Speed Tracking Control of a Permanent-Magnet Synchronous Motor with State and Load Torque Observer. *IEEE Trans. Ind. Electron.* **2000**, *47*, 346–355. [CrossRef]
26. Nguyen, V.; Lee, D.C. Sensorless Control of PMSM Based on Hybrid Extended State Observer. In Proceedings of the 2023 IEEE International Symposium on Sensorless Control for Electrical Drives (SLED), Seoul, Republic of Korea, 16–18 August 2023; pp. 1–6. [CrossRef]
27. Shi, Y.; Wu, Z.; Tong, W. Active Damping Control of Hybrid Stepper Motor Based on IHF-PLL3rd. *Zhongguo Dianji Gongcheng Xuebao/Proc. Chin. Soc. Electr. Eng.* **2023**, *43*, 7298–7307. [CrossRef]
28. Ilka, A.; Murgovski, N. Novel Results on Output-Feedback LQR Design. *IEEE Trans. Autom. Control* **2023**, *68*, 5187–5200. [CrossRef]
29. Vaidyanathan, S.; Madhavan, K. Observer-Based Reduced Order Controller Design for the Stabilization of Large Scale Linear Discrete-Time Control Systems. *Int. J. Comput. Sci. Eng. Inf. Technol.* **2011**, *1*, 85. [CrossRef]
30. Amertet, S.; Gebresenbet, G.; Alwan, H.M. Optimizing the performance of a wheeled mobile robots for use in agriculture using a linear-quadratic regulator. *Robot. Auton. Syst.* **2024**, *174*, 104642. [CrossRef]
31. Kim, S.Y.; Yoon, Y.D.; Sul, S.K. Suppression of Thrust Loss for the Maximum Thrust Operation in the Electric Propulsion Ship. *IEEE Trans. Ind. Appl.* **2009**, *45*, 756–762. [CrossRef]
32. Gao, Z. Scaling and bandwidth-parameterization based controller tuning. In Proceedings of the 2003 American Control Conference, 2003, Denver, CO, USA, 4–6 June 2003; Volume 6, pp. 4989–4996. [CrossRef]
33. Thanh, H.L.N.N.; Huynh, T.T.; Vu, M.T.; Mung, N.X.; Phi, N.N.; Hong, S.K.; Vu, T.N.L. Quadcopter UAVs extended states/disturbance observer-based nonlinear robust backstepping control. *Sensors* **2022**, *22*, 5082. [CrossRef]